The ^{3}He$(e,e'p)^2$H and ^{4}He$(e,e'p)^3$H reactions at high momentum transfer

W.P. Ford[a], R. Schiavilla[b,c], and J.W. Van Orden[b,c]

[a] *Department of Physics, University of Southern Mississippi, Hattiesburg, MS 39406*

[b] *Department of Physics, Old Dominion University, Norfolk, VA 23529, USA*

[c] *Jefferson Lab, Newport News, VA 23606, USA*

arXiv:1401.4399v1 [nucl-th] 17 Jan 2014

(Dated: January 20, 2014)

Abstract

We present updated calculations for observables in the processes ^{3}He$(e,e'p)^2$H, ^{4}He$(e,e'p)^3$H, and ^{4}He$(\vec{e},e'\vec{p})^3$H. This update entails the implementation of improved nucleon-nucleon (NN) amplitudes to describe final state interactions (FSI) within a Glauber approximation and includes full spin-isospin dependence in the profile operator. In addition, an optical potential, which has also been updated since previous work, is utilized to treat FSI for the ^{4}He$(e,e'p)^3$H and ^{4}He$(\vec{e},e'\vec{p})^3$H reactions. The calculations are compared with experimental data and show good agreement between theory and experiment. Comparisons are made between the various approximations in the Glauber treatment, including model dependence due to the NN scattering amplitudes, rescattering contributions, and spin dependence. We also analyze the validity of the Glauber approximation at the kinematics the data is available, by comparing to the results obtained with the optical potential.

I. INTRODUCTION

Recent experiments at Jefferson Lab (JLab) have measured cross sections and polarization observables for the ^{3}He$(e,e'p)^2$H, ^{4}He$(e,e'p)^3$H, and ^{4}He$(\vec{e},e'\vec{p})^3$H reactions at intermediate and large momentum transfers [1–5] . These data have generated considerable interest in the nuclear few-body community, as attested by the series of papers dealing with the description of the proton-knockout mechanism and the treatment of final state interactions (FSI) at GeV energies, which have appeared in the literature in last few years [6–13].

In the present work, we report on a calculation of the two-body electrodisintegration cross sections of ^{3}He and ^{4}He in the wide range of momentum transfers covered by the JLab experiments. This study updates, improves, and extends that of Refs. [14, 15]. As in the earlier work, the nuclear bound states are represented by non-relativistic wave functions, obtained from realistic two- and three-nucleon potentials (the Argonne v_{18} two-nucleon [16] and Urbana IX three-nucleon [17] potentials—the AV18/UIX Hamiltonian) and FSI between the outgoing proton and recoiling bound cluster are treated either in the Glauber approximation for the A=3 and 4 reactions—with inclusion in the associated profile operator of the full spin-isospin dependence of the nucleon-nucleon (NN) elastic scattering amplitude—or, in the case of the A=4 reactions, with an optical potential. Important differences between the present work and that of Refs. [14, 15] are that: i) the NN amplitudes are obtained from the Scattering Analysis Interactive Dial-in (SAID) analysis [18–20] of pn (pp) scattering data at lab kinetic energies ranging from 0.05 (0.05) GeV to 1.3 (3.0) GeV rather than from a parametrization of these amplitudes valid at forward scattering (at small momentum transfers) [21], and ii) the parameters in the optical potential have been adjusted to reproduce, in addition to ^{3}H$(p,p)^3$H elastic and ^{3}H$(p,n)^3$He charge-exchange cross section data, also the induced polarization data recently measured for the ^{4}He$(\vec{e},e'\vec{p})^3$H reaction at JLab [5].

This paper is organized as follows. In Sec. II, we briefly discuss our treatment of FSI both in the Glauber and optical-model approximations, relegating details on the construction of the Glauber profile operator from the NN SAID amplitudes to Appendices A and B. In Sec. III we review the bound-state wave functions, the model for the electromagnetic current operator, and the Monte Carlo methods used in the numerical evaluation of the relevant matrix elements—these methods have already been described in considerable detail in Ref. [14]. In Sec IV we list explicit expressions for the observables of interest to this work.

Finally, in Sec. V we present a detailed discussion of the results, including a comparison between the Glauber and optical-model treatment of FSI in kinematical regimes where both approaches are expected to be valid, and in Sec. VI we summarize our conclusions.

II. FINAL STATE INTERACTIONS

Two different approximations are adopted in the present work to describe FSI in the two-body electrodisintegrations of ^{3}He and ^{4}He: one is based on the Glauber approach [22], while the other, whose application is limited only to processes involving ^{4}He, relies on an optical potential. Both approximations have been discussed in considerable detail in Refs. [14] and [15]: each has limitations as to the energy range where it is expected to be reliable. For completeness, in this section we briefly review them, emphasizing those aspects of the approach which have been improved since the study of Refs. [14, 15].

A. Glauber approach

In this approach the wave function of the final $p+(A-1)$ system is written as

$$\psi(p+^{(A-1)}f;\mathrm{GLB}) = \frac{1}{\sqrt{A}}\sum_{\mathcal{P}} \epsilon_{\mathcal{P}}\, G(A;1\ldots A-1)\, \mathrm{e}^{\mathrm{i}\mathbf{p}\cdot\mathbf{r}_A}\chi_\sigma(A;p)\, \mathrm{e}^{\mathrm{i}\mathbf{p}_f\cdot\mathbf{R}_{1\ldots A-1}}\phi_{\sigma_f}(1\ldots A-1;f)\ , \tag{1}$$

where $\chi_\sigma(p)$ represents a proton in spin state σ, $\phi_{\sigma_f}(f)$ denotes the wave function of the $(A-1)$-system with spin projection σ_f, and $\mathbf{R}_{1\ldots A-1}$ is the center-of-mass position vector of the $A-1$ nucleons in this cluster. The sum over permutations $\mathcal{P}$ of parity $\epsilon_{\mathcal{P}}$ ensures the overall antisymmetry of $\psi(p+^{(A-1)}f;\mathrm{GLB})$.

The operator $G(A;1\ldots A-1)$ inducing FSI can be derived from an analysis of the multiple scattering series by requiring that the struck (fast) nucleon (nucleon A) is undeflected by rescattering processes, and that the nucleons in the residual system (nucleons $1,\ldots,A-1$) act as fixed scattering centers [21]. It is expanded as

$$G = 1 + \sum_{n=1}^{A-1}(-)^n G^{(n)}\ , \tag{2}$$

where $G^{(n)}$ represents the n^{th} rescattering term, and therefore for an A-body system up to

$A-1$ rescattering terms are generally present. The leading single-rescattering term reads

$$G^{(1)}(A;1\ldots A-1)=\sum_{i=1}^{A-1}\theta(z_{iA})\,\Gamma_{iA}(\mathbf{b}_{iA};s_{iA})\ , \tag{3}$$

where z_{iA} and $\mathbf{b}_{iA}$ denote the longitudinal and transverse components of $\mathbf{r}_i-\mathbf{r}_A$ relative to $\hat{\mathbf{p}}$, the direction of the nucleon momentum,

$$z_{iA}\equiv\hat{\mathbf{p}}\cdot(\mathbf{r}_i-\mathbf{r}_A)\ ,\qquad \mathbf{r}_i-\mathbf{r}_A\equiv\mathbf{b}_{iA}+z_{iA}\,\hat{\mathbf{p}}\ , \tag{4}$$

and the step-function $\theta(x)$, $\theta(x)=1$ if $x>0$ and $\theta(x)=0$ if $x<0$, prevents the occurrence of backward scattering for the struck nucleon. The "profile operator" Γ_{iA}, derived from the NN elastic scattering amplitude at the invariant energy $\sqrt{s_{iA}}$, is discussed below. The double- and triple-rescattering terms, relevant for the present study of the ^{3}He$(e,e'p)d$ and ^{4}He$(e,e'p)t$ reactions, are given by

$$G^{(2)}(A;1\ldots A-1)=\sum_{i\neq j=1}^{A-1}\theta(z_{ij})\,\theta(z_{jA})\,\Gamma_{iA}(\mathbf{b}_{iA};s_{iA})\,\Gamma_{jA}(\mathbf{b}_{jA};s_{jA})\ , \tag{5}$$

$$G^{(3)}(A;1\ldots A-1)=\sum_{i\neq j\neq k=1}^{A-1}\theta(z_{ij})\,\theta(z_{jk})\,\theta(z_{kA})\,\Gamma_{iA}(\mathbf{b}_{iA};s_{iA})\,\Gamma_{jA}(\mathbf{b}_{jA};s_{jA})\,\Gamma_{kA}(\mathbf{b}_{kA};s_{kA})\ , \tag{6}$$

where the product of θ-functions ensures the correct sequence of rescattering processes in the forward hemisphere.

The profile operator Γ_{ij} is related to the NN scattering amplitude, denoted as $F_{ij}(\mathbf{k};s)$, via the Fourier transform

$$\Gamma_{ij}(\mathbf{b};s)=\frac{1}{2\pi\mathrm{i}\,p}\int\mathrm{d}^2\mathbf{k}\,\mathrm{e}^{-\mathrm{i}\mathbf{k}\cdot\mathbf{b}}F_{ij}(\mathbf{k};s)\ , \tag{7}$$

where, in the eikonal limit, the momentum transfer $\mathbf{k}$ is perpendicular to $\mathbf{p}$. The isospin symmetry of the strong interactions allows one to express F_{ij} as

$$F_{ij}=F_{ij,+}+F_{ij,-}\boldsymbol{\tau}_i\cdot\boldsymbol{\tau}_j\ , \tag{8}$$

where the $F_{ij,\pm}$ are related to the physical amplitudes for pp and pn scattering (see below). The invariant energy $\sqrt{s_{iA}}$ is determined as follows [14]. Nucleon A denotes the knocked-out nucleon with momentum $\mathbf{p}_A$=$\mathbf{p}$ and energy E_A=E ($\mathbf{p}$ and E are the momentum and energy

of the outgoing proton in the lab frame), while nucleons $1,\ldots,A-1$, making up the bound cluster (d or t), have momenta $\mathbf{p}_1,\ldots,\mathbf{p}_{A-1}$, with $\mathbf{p}_1+\cdots+\mathbf{p}_{A-1}$=$\mathbf{p}_f$ ($\mathbf{p}_f$ is the momentum of the recoiling cluster in the lab frame). The invariant energy $\sqrt{s_{iA}}$, i=$1,\ldots,A-1$, is obtained from

$$\begin{aligned} s_{iA} &= (E_i+E_A)^2-(\mathbf{p}_i+\mathbf{p}_A)^2 \\ &\simeq 2\,m^2+2\,E\,\sqrt{\mathbf{p}_f^2/(A-1)^2+m^2}-2\,\mathbf{p}\cdot\mathbf{p}_f/(A-1)\ , \end{aligned} \tag{9}$$

where in the second line the nucleons $1,\ldots,A-1$ in the recoiling cluster are assumed to share its momentum equally, $\mathbf{p}_i\simeq\mathbf{p}_f/(A-1)$. The momenta of nucleon A and nucleon i, i=$1,\ldots,A-1$, after rescattering are $\mathbf{p}-\mathbf{k}$ and $\mathbf{p}_f/(A-1)+\mathbf{k}$. The $A-2$ spectator nucleons ($j\neq i$) have each momentum $\mathbf{p}_f/(A-1)$. The pair iA "rescattering frame"we refer to in the following is defined as that in which nucleon A and nucleon i have initial momenta $\mathbf{p}$ and $\mathbf{p}_f/(A-1)$ and final momenta $\mathbf{p}-\mathbf{k}$ and $\mathbf{p}_f/(A-1)+\mathbf{k}$, respectively.

We adopt the notation of Ref. [14] and parameterize the NN scattering amplitude in the c.m. frame as

$$(2\mathrm{i}\,\overline{p})^{-1}\,\overline{F}_{ij}^{\,NN}(\,\overline{\mathbf{k}},s)=\sum_{m=1}^{5}\overline{F}_m^{\,NN}(\overline{\mathbf{k}}^{\,2},s)\overline{O}_{ij}^{\,m}\ , \tag{10}$$

where $\overline{\mathbf{p}}$ and $\overline{\mathbf{p}}\,'$ denote the initial and final nucleon momenta, respectively, the $\overline{F}_m^{\,NN}$'s are functions of the invariant energy $\sqrt{s}$ and momentum transfer $\overline{\mathbf{k}}^{\,2}$ (with $\overline{\mathbf{k}}=\overline{\mathbf{p}}-\overline{\mathbf{p}}\,'$), and the five operators $\overline{O}_{ij}^{\,m}$, including central, single and double spin-flip terms, are those listed in Eq. (3.11) of Ref. [14]. The overline is to indicate that the quantities above are in the c.m. frame.

In Ref. [14] we used for the functions $\overline{F}_m^{\,NN}$ the Gaussian parameterizations obtained by Wallace in 1981 [21]. In the present work, instead, we derive them from the SAID analysis [18–20] of NN elastic scattering data from threshold up to lab kinetic energies of 3 GeV (pp) and 1.3 GeV (pn). In Appendix A we discuss how the Wallace form of the amplitudes is obtained from the SAID helicity amplitudes.

Once the amplitude in Eq. (10) has been determined in the c.m. frame, it is necessary to boost it to the rescattering frame. This is carried out with the procedure described in Refs. [14, 23], which consists of two steps. First, we introduce an invariant representation of the amplitude,

$$\mathcal{F}_{ij}^{NN}=\sum_{m=1}^{5}\mathcal{F}_m^{NN}(s,t)\Lambda_{ij}^m\ , \tag{11}$$

where the five operators $\Lambda_{ij}^{m=1,\ldots,5}$ are $1\,,\ \gamma_i^\mu\,\gamma_{j,\mu}\,,\ \sigma_i^{\mu\nu}\,\sigma_{j,\mu\nu}\,,\ \gamma_i^5\,\gamma_j^5\,,\ \gamma_i^5\,\gamma_i^\mu\,\gamma_j^5\,\gamma_{j,\mu}$, and determine the invariant functions $\mathcal{F}_m^{NN}(s,t)$ from the $\overline{F}_m^{NN}$'s in the c.m. frame as in Ref. [14]—however, the momentum transfer dependence of the matrix $\overline{M}_{mn}(\overline{p},\overline{\mathbf{k}}^2)$ in Eq. (3.16) of Ref. [14], which was neglected in that work, is now fully retained.

Next, the scattering amplitude in the rescattering frame is obtained from

$$\chi^\dagger_{\sigma'_i}\chi^\dagger_{\sigma'_j}\left[(2\mathrm{i}\,p)^{-1}\,F_{ij}^{NN}(\mathbf{k},s)\right]\chi_{\sigma_i}\chi_{\sigma_j} = \overline{u}_{\sigma'_i}(\mathbf{p}-\mathbf{k})\overline{u}_{\sigma'_j}(\mathbf{p}_f/(A-1)+\mathbf{k})\mathcal{F}_{ij}^{NN}u_{\sigma_i}(\mathbf{p})u_{\sigma_j}(\mathbf{p}_f/(A-1))\,, \tag{12}$$

where the u_σ are (positive-energy) Dirac spinors with $\overline{u}_\sigma \equiv u_\sigma^\dagger\gamma^0$, and χ_σ are two-component Pauli spinors. In practice, the dependence upon $\mathbf{p}_f/(A-1)$ in the spinors of particle j is neglected (in this limit, the rescattering and lab frames for the interacting NN pair coincide). This is justified as long as $p_f/(A-1)$ is not too large relative to p, the momentum of the fast ejected proton, a condition satisfied at low missing momenta p_f in the experiments of Refs. [1–3]. The resulting $F_{ij}^{NN}(\mathbf{k},s)$ has central, single and double spin-flip terms, and is given explicitly in Appendix B.

Finally, carrying out the (two-dimensional) Fourier transform in Eq. (7) leads to the profile operator

$$\begin{aligned}\Gamma_{ij}(\mathbf{b};s) = {}& \Gamma_{ij}^{(1)}(b;s) + \Gamma_{ij}^{(2)}(b;s)\,\boldsymbol{\sigma}_i\cdot\boldsymbol{\sigma}_j + \left[\Gamma_{ij}^{(3)}(b;s)\,\boldsymbol{\sigma}_i + \Gamma_{ij}^{(4)}(b;s)\,\boldsymbol{\sigma}_j\right]\cdot\mathbf{b}\times\hat{\mathbf{p}} \\ & + \Gamma_{ij}^{(5)}(b;s)\,\boldsymbol{\sigma}_i\cdot\mathbf{b}\;\boldsymbol{\sigma}_j\cdot\mathbf{b} + \Gamma_{ij}^{(6)}(b;s)\,\boldsymbol{\sigma}_i\cdot\hat{\mathbf{p}}\;\boldsymbol{\sigma}_j\cdot\hat{\mathbf{p}} + \Gamma_{ij}^{(7)}(b;s)\,\boldsymbol{\sigma}_i\cdot\mathbf{b}\;\boldsymbol{\sigma}_j\cdot\hat{\mathbf{p}} \\ & + \Gamma_{ij}^{(8)}(b;s)\,\boldsymbol{\sigma}_i\cdot\hat{\mathbf{p}}\;\boldsymbol{\sigma}_j\cdot\mathbf{b}\;,\end{aligned} \tag{13}$$

where the isospin-dependent operators $\Gamma_{ij}^{(m)}$, $m=1,\ldots,8$, are given by

$$\Gamma_{ij}^{(m)}(b;s) = \Gamma_{+}^{(m)}(b;s) + \Gamma_{-}^{(m)}(b;s)\,\boldsymbol{\tau}_i\cdot\boldsymbol{\tau}_j\;. \tag{14}$$

The profile functions $\Gamma_{\pm}^{(m)}$ are related to those corresponding to pp and pn elastic scattering, obtained in Appendix B, via

$$\Gamma_{\pm}^{(m)} = \left(\Gamma_{pp}^{(m)} \pm \Gamma_{pn}^{(m)}\right)/2\;. \tag{15}$$

B. Optical potential

To describe FSI effects in the ^{4}He$(e,e'p)^3$H and ^{4}He$(\vec{e},e'\vec{p})^3$H reactions, we also use an optical potential [15, 24, 25]. In this case, the $p\,^3$H wave function reads

$$\psi^{(-)}_{\mathbf{k}\sigma;\sigma_3}(p+{}^3\mathrm{H};\mathrm{OPT}) = \frac{\mathrm{e}^{\mathrm{i}(\mathbf{p}+\mathbf{p}_3)\cdot\mathbf{R}_{1\ldots4}}}{\sqrt{4}} \sum_{\mathcal{P}} \epsilon_{\mathcal{P}} \left[\eta^{(-)}_{\mathbf{k}\sigma}(i;p)\phi_{\sigma_3}(jkl;{}^3\mathrm{H}) + \eta^{(-)}_{\mathbf{k}\sigma}(i;n)\phi_{\sigma_3}(jkl;{}^3\mathrm{He})\right] , \tag{16}$$

where σ and σ_3 are the spectator nucleon and bound cluster spin projections, $\mathbf{k}$ and $\mathbf{p}+\mathbf{p}_3$ are their relative and total momenta, respectively.

The spectator wave functions $\eta(i;p/n)$ are obtained from the linear combinations $[\eta(i;T=1)+/-\eta(i;T=0)]/2$, where T=0,1 denotes the total isospin of the 1+3 clusters. The latter are taken to be the scattering solutions of a Schrödinger equation containing a complex, energy-dependent optical potential of the form

$$v^{\mathrm{opt}}_T(T_{\mathrm{rel}}) = [v^c(r;T_{\mathrm{rel}}) + (4T-3)v^{c\tau}(r;T_{\mathrm{rel}})] + [v^b(r;T_{\mathrm{rel}}) + (4T-3)v^{b\tau}(r;T_{\mathrm{rel}})]\,\mathbf{l}\cdot\mathbf{s} , \tag{17}$$

where T_{rel} is the relative energy between clusters i and jkl, and $\mathbf{l}$ and $\mathbf{s}$ are the orbital and spin angular momenta of nucleon i, respectively. The imaginary part of v^{opt}_T accounts for the loss of flux in the $p\,^3$H and $n\,^3$He states due to their coupling to the dd, three- and four-body breakup channels of ^{4}He. Note that the n+^{3}He component in the scattering wave function $\psi^{(-)}(p+{}^3\mathrm{H})$ vanishes unless the isospin-dependent (charge-exchange) terms in v^{opt} are included. In the results presented in Sec. V, all partial waves are retained in the expansion of $\eta(i;T)$, with full account of interaction effects in those with relative orbital angular momentum $l \leq 17$. It has been explicitly verified that the numerical importance of FSI in higher partial waves is negligible.

The central v^c and $v^{c\tau}$, and spin-orbit v^b and $v^{b\tau}$ terms have standard Woods-Saxon and Thomas functional forms. The parameters of v^c and v^b were determined by fitting $p+^3$H elastic cross section data in the lab energy range T_{lab}=(160–600) MeV, see Ref. [24] for a listing of their values. The parameters of the $v^{c\tau}$ and $v^{b\tau}$ terms have been constrained by fitting p+^{3}H $\to$ n+^{3}He charge-exchange cross section data at T_{lab}=57 MeV and 156 MeV [25] and the induced polarization P_y measured in the ^{4}He$(e,e'\vec{p})^3$H reaction [5]. The charge-exchange central term has a real part given by $[7.60-0.033\,T_{\mathrm{lab}}(\mathrm{MeV})]$ MeV with radius and diffuseness of 1.2 fm and 0.15 fm and an imaginary part given by $[0.893-0.0025\,T_{\mathrm{lab}}(\mathrm{MeV})]$ MeV with radius and diffuseness of 1.8 fm and 0.2 fm, while the charge-exchange spin-orbit

term is taken to be purely real, with a depth parameter depending logarithmically on $T_{\rm lab}$, $[-15.0 + 1.5 \log T_{\rm lab}({\rm MeV})]$ in MeV, and with radius and diffuseness having the values 1.2 fm and 0.15 fm, respectively (note that in Ref. [15] the sign of the depth parameter of this term had been reported erroneously with the opposite sign).

III. CALCULATION

In this section we give, for completeness, a brief summary of those aspects of the calculations, relating to the bound cluster wave functions, nuclear electromagnetic current, and Monte Carlo methods used in evaluating the matrix elements, which have already been reviewed in considerable detail in Refs. [14, 15] and references therein.

The bound states of the three- and four-nucleon systems are represented by variational wave functions, obtained with the hyperspherical-harmonics (HH) technique [26] from a realistic Hamiltonian consisting of the Argonne v_{18} [16] and Urbana-IX [17] (AV18/UIX) potentials. These potentials and the resulting wave functions have been shown to account successfully at a quantitative level for a wide variety of three- and four-nucleon properties, such as binding energies and charge radii [26].

The nuclear electromagnetic current includes one- and two-body components. The one-body operators, listed in Ref. [14], are derived from an expansion of the covariant single-nucleon current [27]. The two-body operators used in the present work are discussed in the review paper [28] (and references therein). The leading terms are derived from the static part of the AV18 potential, which is assumed to be due to exchanges of effective pseudo-scalar (π-like) and vector (ρ-like) mesons. The corresponding charge and current operators are constructed from non-relativistic reductions of Feynman amplitudes with the π-like and ρ-like effective propagators projected out of the central, spin-spin and tensor components of the AV18. Additional (short-range) currents result from minimal substitution in its momentum-dependent components. These charge and current operators contain no free parameters, and their short-range behavior is consistent with that of the AV18. The (purely transverse) two-body currents associated with $M1$-excitation of Δ resonances in the intermediate state, and from $\rho\pi\gamma$ and $\omega\pi\gamma$ transition mechanisms are also included. As documented in Refs. [28–30], these charge and current operators reproduce quite well a variety of few-nucleon electromagnetic observables, ranging from elastic form factors to

low-energy radiative capture cross sections to the quasi-elastic response in inclusive (e, e') scattering at intermediate energies.

The Höhler parameterization [31] is used for the electromagnetic form factors of the nucleon. In the analysis of the ^{4}He$(\vec{e}, e'\vec{p})^3$H experiment, however, at the highest Q^2 values of 1.6 (GeV/c)^2 and 2.6 (GeV/c)^2 the proton electric and magnetic form factors are taken from the parameterization obtained in Ref. [32] by fitting G_{Mp} data and the ratio G_{Ep}/G_{Mp} recently measured at JLab [33].

Finally, the numerical evaluation of the relevant matrix elements is carried out by a combination of Monte Carlo methods and standard quadrature techniques, described for the case of A=3 in Ref. [14]. This hybrid approach is easily generalized to the A=4 case: indeed, it was already used in the calculations reported in Ref. [15]. The resulting predictions are numerically "exact", apart from small statistical errors due to the Monte Carlo integration, and therefore suffer from no further approximations beyond those inherent to the treatment of FSI and nuclear electromagnetic currents.

IV. OBSERVABLES

For clarity we briefly recap the observables of interest for this calculation. More details can be found in Refs. [14, 15] for observables relevant to the ^{3}He$(e, e'p)^2$H and ^{4}He$(e, e'p)^3$H reactions, respectively.

The five-fold differential cross section for the $^Ai(e, e'p)^{(A-1)}f$ process is given as

$$\frac{d^5\sigma}{dE'_e d\Omega'_e d\Omega} = p\, E\, \sigma_{\rm Mott}\, f_{\rm rec} \frac{m}{E}\frac{m_f}{E_f} \left[v_L R_L + v_T R_T + v_{LT}\, R_{LT} \cos(\phi) + v_{TT} R_{TT} \cos(2\phi)\right], \quad (18)$$

where E'_e is the energy of the final electron, Ω'_e and Ω are, respectively, the solid angles of the final electron and ejected proton, m_f is the rest mass of the (A–1)-cluster, $\mathbf{p}$ and E ($\mathbf{p}_f$ and E_f) are the momentum and energy of the proton ((A–1)-cluster), ϕ is the angle between the electron scattering plane and the plane defined by $\mathbf{q}$ and $\mathbf{p}$, and the recoil factor is defined by its inverse

$$f_{\rm rec}^{-1} = \left| 1 - \frac{p_f\, E}{p\, E_f} \hat{\mathbf{p}} \cdot \hat{\mathbf{p}}_f \right|. \quad (19)$$

For a derivation of Eq. (18), the definition of $\sigma_{\rm Mott}$ and of the (standard) electron kinematic factors, v_α, where $\alpha = L, T, LT, TT$, see Ref. [34]. The nuclear response functions are given in Ref. [14].

The longitudinal-transverse asymmetry A_{LT} is obtained from the differential cross sections

$$A_{LT} = \frac{\sigma(\phi = 0^\circ) - \sigma(\phi = 180^\circ)}{\sigma(\phi = 0^\circ) + \sigma(\phi = 180^\circ)} = \frac{v_{LT} R_{LT}}{v_L R_L + v_T R_T + v_{TT} R_{TT}}, \tag{20}$$

where $\sigma(\phi)$ represents the differential cross section in Eq. (18).

In parallel kinematics, where the electron three-momentum transfer $\mathbf{q}$ and the missing momentum $\mathbf{p}_m$ (defined as $\mathbf{p}_m = -\mathbf{p}_f = \mathbf{p} - \mathbf{q}$) are parallel, the polarization transfers P'_x and P'_z are given by

$$P'_x = \frac{v_{LT'} R^t_{LT'}}{v_L R_L + v_T R_T} \ , \qquad P'_z = \frac{v_{TT'} R^l_{TT'}}{v_L R_L + v_T R_T} \ , \tag{21}$$

where the response functions $R^t_{LT'}$ and $R^l_{TT'}$ and electron kinematical factors $v_{LT'}$ and $v_{TT'}$ read [35]

$$R^t_{LT'} = 2\sqrt{2} \sum_{m_3} \mathrm{Im}\Big[\langle p + {}^3\mathrm{H}; +\hat{\mathbf{x}}, m_3 |\ \rho(q\hat{\mathbf{z}})\ | {}^4\mathrm{He} \rangle \, \langle p + {}^3\mathrm{H}; +\hat{\mathbf{x}}, m_3 |\ j_y(q\hat{\mathbf{z}})\ | {}^4\mathrm{He} \rangle^* \Big] \ , \tag{22}$$

$$R^l_{TT'} = 2 \sum_{m_3} \mathrm{Im}\Big[\langle p + {}^3\mathrm{H}; +\hat{\mathbf{z}}, m_3 |\ j_x(q\hat{\mathbf{z}})\ | {}^4\mathrm{He} \rangle \, \langle p + {}^3\mathrm{H}; +\hat{\mathbf{z}}, m_3 |\ j_y(q\hat{\mathbf{z}})\ | {}^4\mathrm{He} \rangle^* \Big] \ , \tag{23}$$

$$v_{LT'} = \frac{1}{\sqrt{2}} \frac{Q^2}{q^2} \tan(\theta_e/2) \ , \qquad v_{TT'} = \tan(\theta_e/2) \sqrt{\frac{Q^2}{q^2} + \tan^2(\theta_e/2)} \ . \tag{24}$$

and θ_e and $Q^2 = q^2 - \omega^2$ are, respectively, the electron scattering angle and four-momentum transfer. In the above equations, $|\,{}^4\mathrm{He}\rangle$ represents the ^{4}He ground state, while $|\,p + {}^3\mathrm{H}; +\hat{\mathbf{x}}, m_3\rangle$ and $|\,p + {}^3\mathrm{H}; +\hat{\mathbf{z}}, m_3\rangle$ represent the $p + {}^3$H final scattering states with the proton spin projection along either the $\hat{\mathbf{x}}$ or the $\hat{\mathbf{z}}$ directions, respectively, and with the ^{3}H in spin projection m_3. The momentum transfer $\mathbf{q}$ has been taken along the $\hat{\mathbf{z}}$ direction, which also defines the quantization axis of the proton and ^{3}H spins. Then, the $|p + {}^3\mathrm{H}; +\hat{\mathbf{x}}, m_3\rangle$ state, having the proton polarized in the $\hat{\mathbf{x}}$ direction, is written as

$$|p + {}^3\mathrm{H}; +\hat{\mathbf{x}}, m_3\rangle = \frac{1}{\sqrt{2}} \, |p + {}^3\mathrm{H}; +\hat{\mathbf{z}}, m_3\rangle + \frac{1}{\sqrt{2}} \, |p + {}^3\mathrm{H}; -\hat{\mathbf{z}}, m_3\rangle \ , \tag{25}$$

and the amplitudes $\langle p + {}^3\mathrm{H}; \pm\hat{\mathbf{z}}, m_3 |\ O(q\hat{\mathbf{z}})\ | {}^4\mathrm{He} \rangle$ are calculated for all possible combinations of proton and ^{3}H spin projections and of transition operators $O(q\hat{\mathbf{z}})$ with the methods discussed in the previous section.

Lastly, the induced polarization P_y is defined as

$$P_y = \frac{v_{LT}\,\Delta R_{LT}}{v_L R_L + v_T R_T} \tag{26}$$

where the ΔR_{LT} response function is defined as

$$\Delta R_{LT} = 2\sqrt{2}\sum_{m_3} \mathrm{Re}\Big[\langle p\,{+}^3\mathrm{H}; +\hat{\mathbf{y}}, m_3 |\, \rho(q\hat{\mathbf{z}})\, |^4\mathrm{He}\rangle \langle p\,{+}^3\mathrm{H}; +\hat{\mathbf{y}}, m_3 |\, j_x(q\hat{\mathbf{z}})\, |^4\mathrm{He}\rangle^* - \langle p\,{+}^3\mathrm{H}; -\hat{\mathbf{y}}, m_3 |\, \rho(q\hat{\mathbf{z}})\, |^4\mathrm{He}\rangle \langle p\,{+}^3\mathrm{H}; -\hat{\mathbf{y}}, m_3 |\, j_x(q\hat{\mathbf{z}})\, |^4\mathrm{He}\rangle^*\Big]\,, \tag{27}$$

and in the states $|\,p\,{+}^3\mathrm{H}; \pm\hat{\mathbf{y}}, m_3\rangle$ the proton polarization is along the $\pm\hat{\mathbf{y}}$ direction (note that in parallel kinematics, the proton and electron scattering planes concide, and are taken here as the xz-plane).

V. RESULTS

In this section we compare the results of our calculations to experimental data. In addition we compare various model-dependent effects, and discuss how these affect the results.

A. ^{3}He$(e,e'p)^2$H

As in Ref. [14] the predicted cross section and asymmetry are compared with experimental data taken at JLab (E89-044) [1]. For the $^3\mathrm{He}(e,e'p)^2\mathrm{H}$ reaction all observables are plotted as function of the missing momentum p_m. The calculated cross sections are compared to experimental data for ϕ=180° in Fig. 1 and for ϕ=0° in Fig. 2. The longitudinal-transverse asymmetry is obtained from these cross sections via Eq. (20), and its comparison to experiment is shown in Fig. 3.

In Figs. 1–3, the curves labeled PWIA represent the results obtained in the plane-wave impulse-approximation disregarding all FSI. The PWIA overpredicts the data at low p_m and underpredicts them at high p_m. The curves labeled "GLB(1+2) No MEC" represent the results obtained in the Glauber approximation with single and double rescattering, but neglecting contributions from meson exchange currents (MEC). By accounting for FSI, we note a significant improvement in describing the experimental cross-section values. Inclusion of MEC contributions, curves labeled as "GLB(1+2) With MEC", further improves the comparison with the data. While in Figs. 1 and 2 the MEC effects appear small in comparison

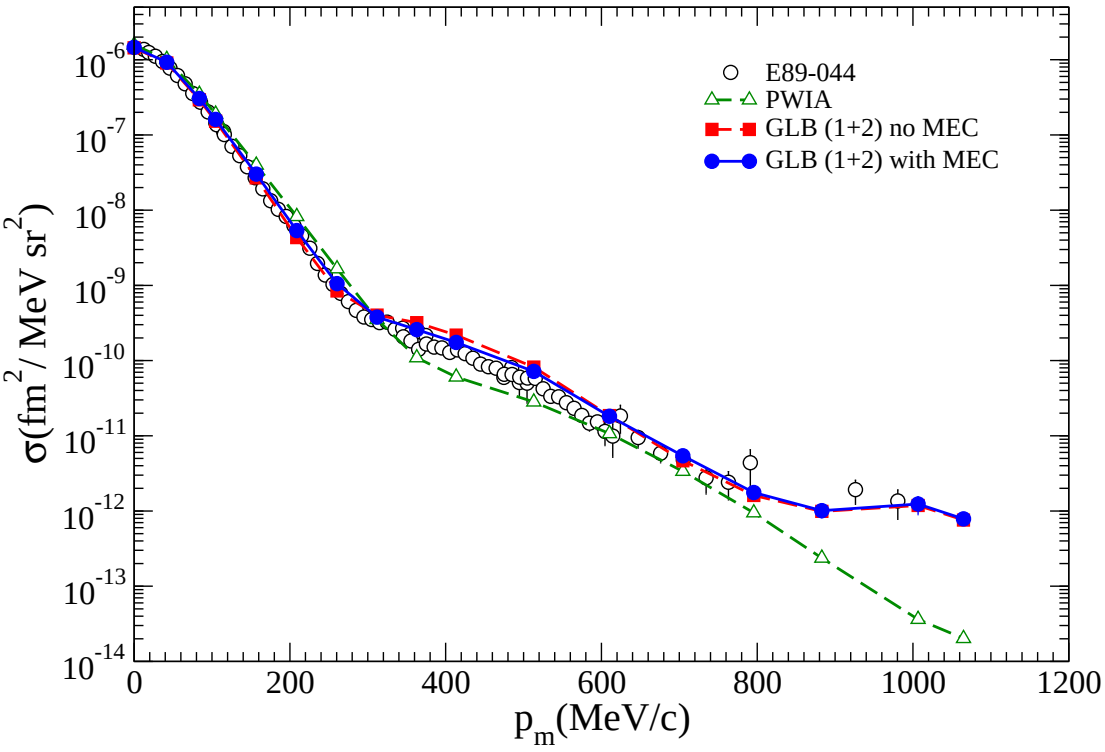

FIG. 1. (Color online) Differential cross sections for the ^{3}He$(e,e'p)^2$H reaction at ϕ=180°. The experimental data are compared with the plane-wave-impule-approximation (PWIA), and with the full single and double rescattering Glauber approximation with MEC (GLB(1+2) With MEC) and without MEC (GLB(1+2) No MEC). The profile operator in the Glauber approximation is derived from NN scattering amplitudes (including central, single-spin flip and double-spin flip terms), boosted from the c.m. frame to the rescattering (lab) frame. Statistical Monte Carlo errors are smaller than the symbols, and lines drawn to guide the eye.

to the FSI, it is clear that they improve the predictions, especially at intermediate values of missing momentum. In Fig. 3, where the asymmetry is shown, the effects are even more pronounced. We note again the inability of the PWIA to successfully account for the experimental features, except for very low values of missing momentum. The structure of the data is clearly dominated by FSI as the missing momentum is increased, and the importance of the MEC is again notable. Indeed at intermediate values of p_m the MEC

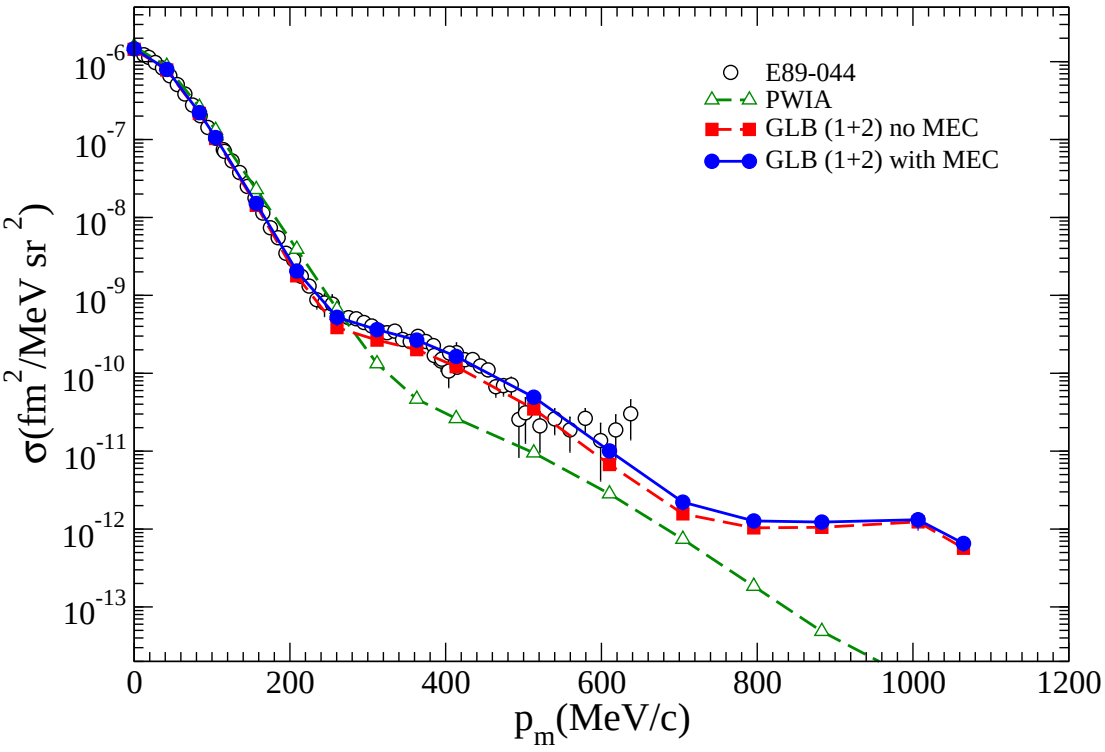

FIG. 2. (Color online) Same as Fig. 1, but at ϕ=0°.

contribution is of comparable strength as the FSI. When calculating A_{LT}, we are taking a difference between the cross sections shown in Fig. 1 and Fig. 2, where in the former the MEC suppress the results, and in the latter the MEC enhance them. So even though this is a small effect in the individual cross sections, it becomes quite large when taking their difference.

We next want to investigate model-dependent effects due to the NN scattering amplitudes. In order to compare the various effects, calculations were performed for a variety of cases, and comparisons are presented in Figs. 4–8. Specifically, we are interested in quantifying the role of spin dependence in the FSI, which this work facilitates well, since all spin dependence is retained in the Glauber profile operator. These cases were all calculated for the same random walk in the Monte Carlo integration, and are not compared to experimental data. Since we have already investigated MEC contributions and noted their

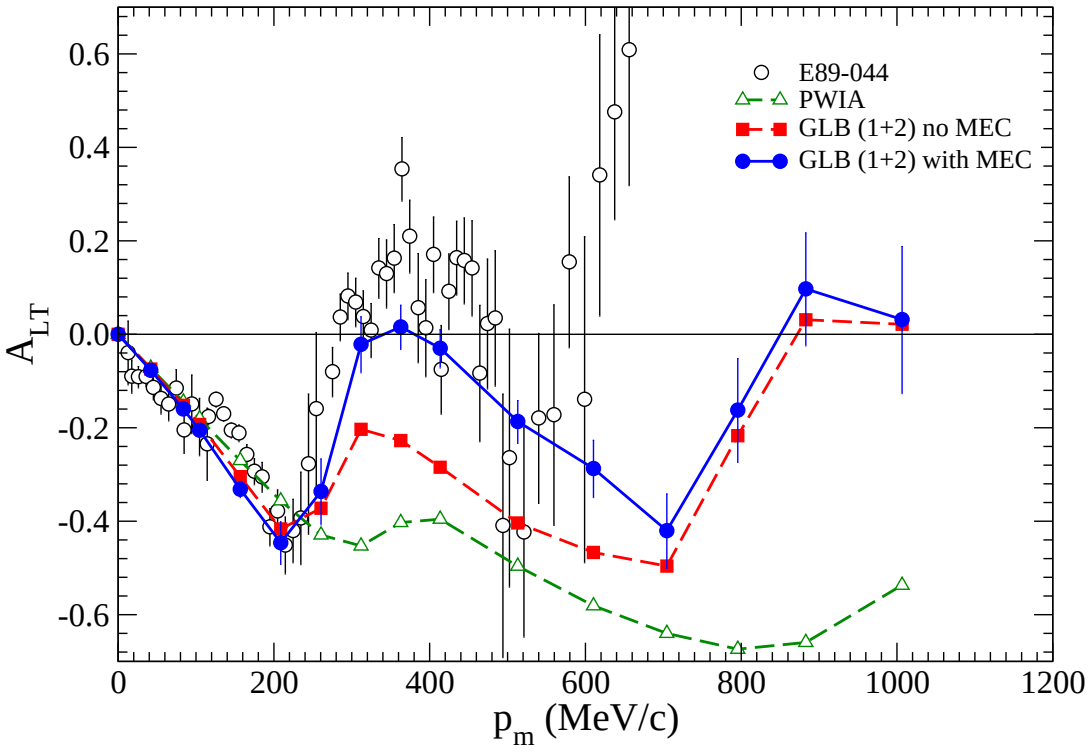

FIG. 3. (Color online) Same as Fig. 1, but for the longitudinal-transverse asymmetry.

importance in the discussion above, all results below include them. The cases we investigate are:

1. Curves labeled "GLB(1+2) Full F" correspond to the Glauber approximation with single and double rescattering and include the full spin dependence in the NN scattering amplitudes.

2. Curves labeled "GLB(1)" include only single scattering in the Glauber approximation, but still incorporate the full spin dependence in the NN scattering amplitudes.

3. Curves labeled "GLB(1+2) Central F" correspond to Glauber single and double rescattering, but with all spin dependent terms turned off in the NN scattering amplitudes, that is, in Eq. (10) we set $\overline{F}_m^{NN}(\overline{\mathbf{k}}^2, s) = 0$ for m=2–5, so that only the central term $\overline{F}_1^{NN}(\overline{\mathbf{k}}^2, s)$ contributes.

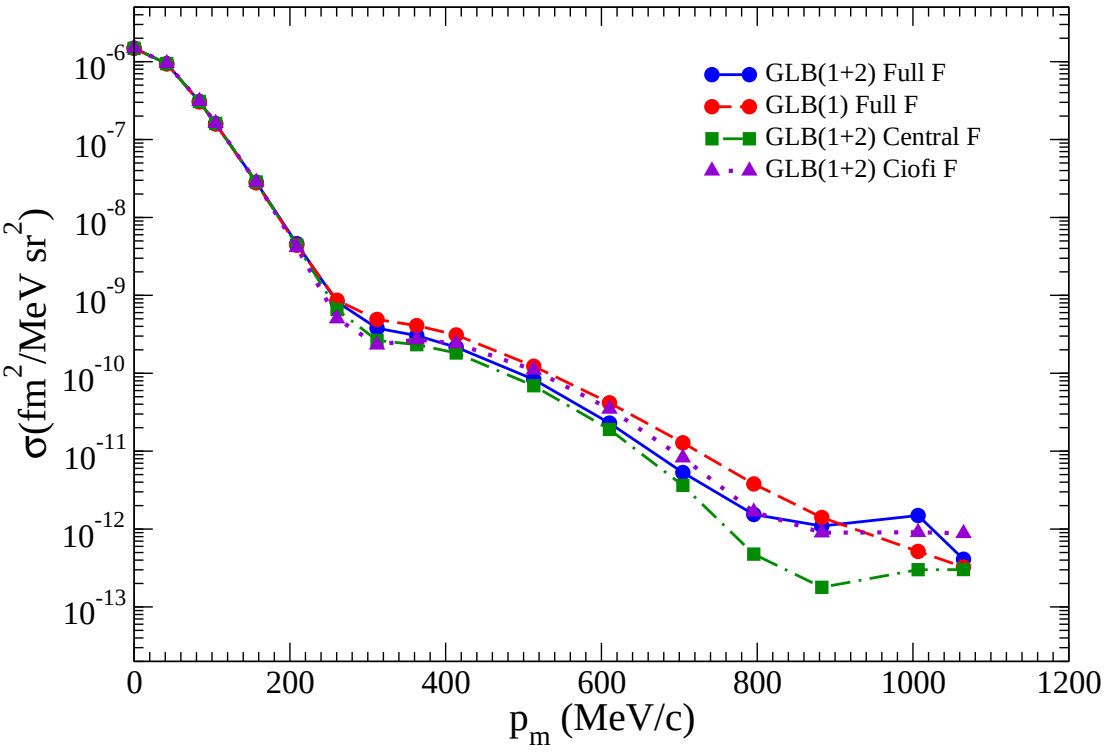

FIG. 4. (Color online) Differential cross sections for the ^{3}He$(e,e'p)^2$H reaction at ϕ=180° obtained in various approximation schemes, see text for descriptions of the approximations. Lines are drawn to guide the eye.

4. Curves labeled "GLB(1+2) Ciofi F" correspond to using a common NN parametrization given in Eq. (A1), which includes no explicit spin dependence. The parameterization is described in Appendix A. It should be noted, however, that when fitting a spin independent amplitude to experimental data, spin dependence can implicitly enter the parameterization, which causes some ambiguity when trying to determine its role in FSI.

In Figs. 4 and 5 we show the differential cross sections calculated at ϕ= 180° and ϕ=0°, respectively. Since these are semilog plots, we also plot ratios of the various cases to the full double rescattering, fully spin dependent calculation, case 1. These are shown in Figs. 6 and 7, again for ϕ=180° and ϕ=0°, respectively. In Fig. 8 we plot the longitudinal-transverse

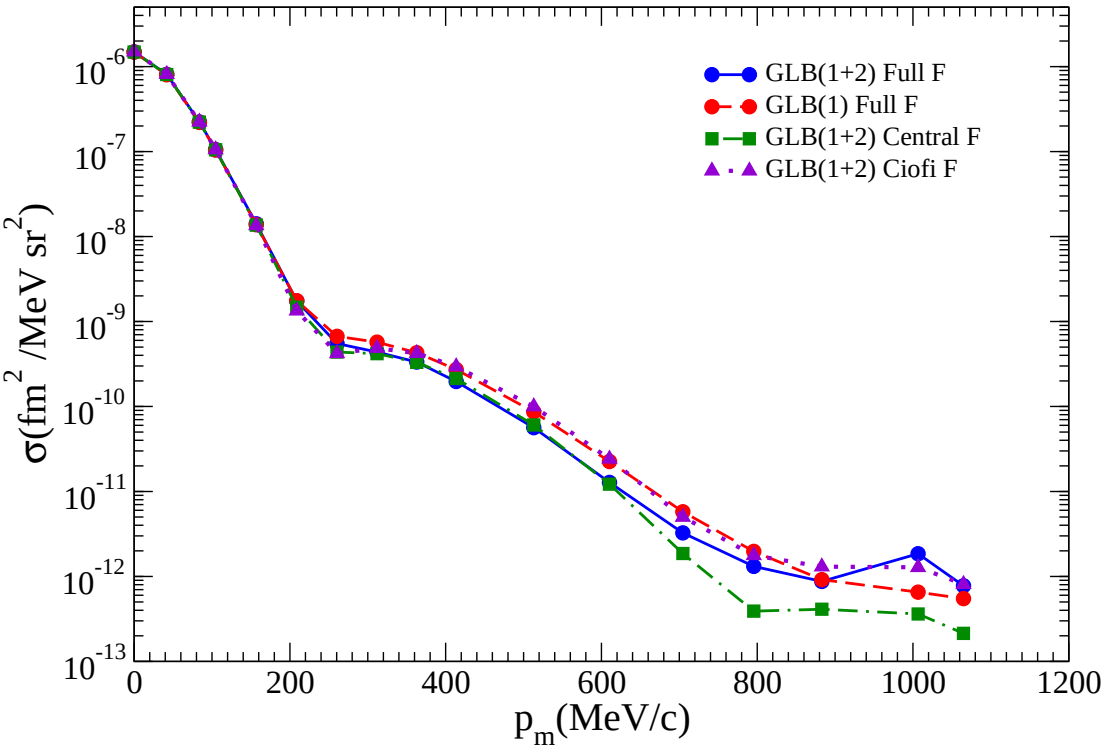

FIG. 5. (Color online) Same as Fig. 4, but at ϕ=0°.

asymmetry for comparison of the four cases. In these figures we first note the necessity of including the double rescattering in the Glauber approximation, case 2. At all but the lowest missing momentum, where FSI are negligible, we see that the single scattering approximation leads to a significant deviation for $p_m > 200$ MeV/c. Next we observe the effect of "turning off" the spin dependent contributions the NN amplitudes, case 3. Here again we note significant deviations from the full result. Finally, we turn to case 4 and note similar deviations as in case 3 for $p_m \lesssim 400$ MeV/c. However, at larger p_m where FSI effects become quite important, predictions for cases 3 and 4 differ significantly from each other—see Figs. 6–7—which can be traced back to differences between the central amplitudes of cases 3 and 4 (see discussion in Appendix A).

It is interesting to point out that for the asymmetry, shown in Fig. 8, the effects are similar for each of the four cases, however, we note that there is no significant deviation for the

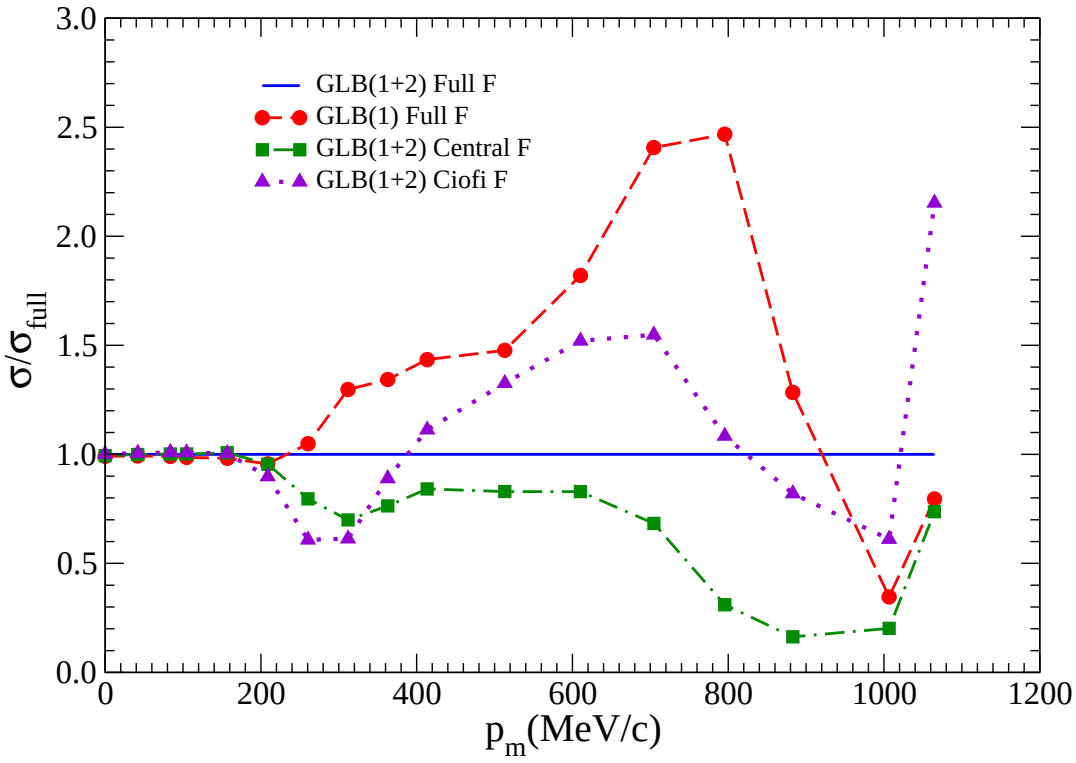

FIG. 6. (Color online) Ratios of differential cross sections as shown in Fig. 4.

single and double rescattering up to $p_m \approx 600$ MeV/c. This implies that the effects of double rescattering, so pronounced in the differential cross section for $p_m > 200$ MeV/c, cancel when calculating the asymmetry. This is similar to the above discussion regarding MEC, and again is due to taking differences of cross sections, except here the double scattering contribution increases the cross sections for both kinematics so when taking the difference this increase is canceled out.

B. ^{4}He$(e,e'p)^3$H

We now turn our attention to the observables calculated for the ^{4}He$(e,e'p)^3$H reaction. In this case we utilize both the Glauber description of FSI as well as an optical potential. We begin by discussing JLab experiment E97-111, for which preliminary data have been published in Ref. [2]—these preliminary data, which only include statistical errors, are shown

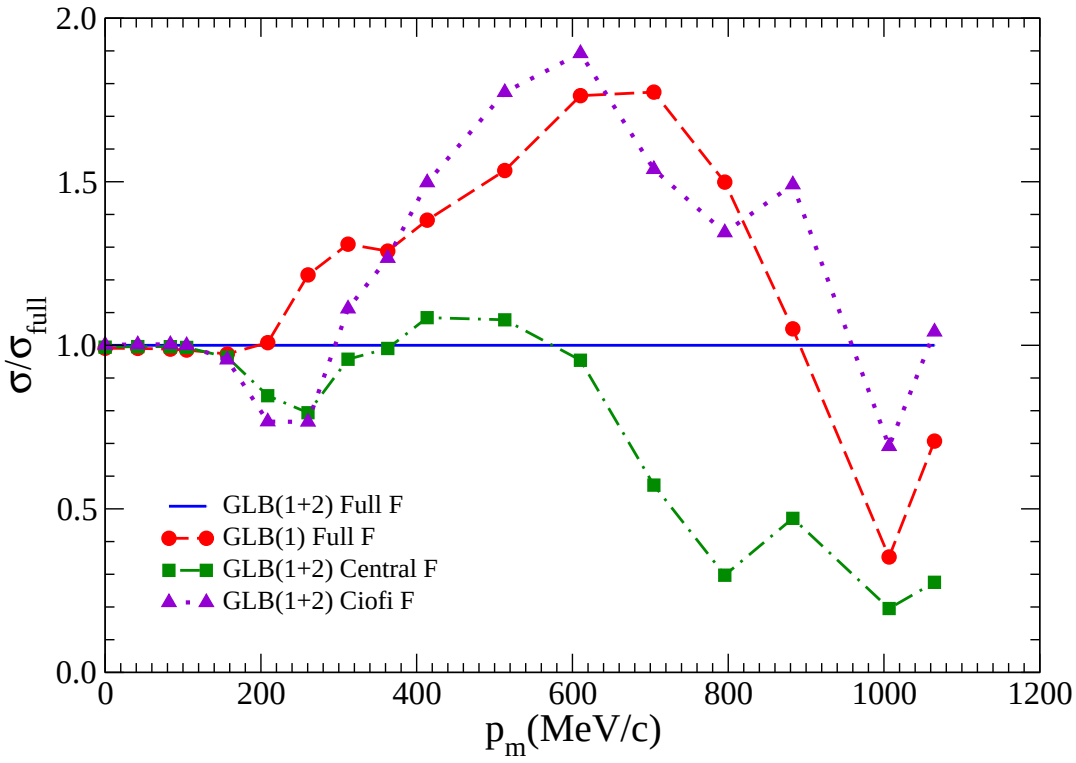

FIG. 7. (Color online) Ratios of differential cross sections as shown in Fig. 5.

in the figures below. The experiment measured cross sections for the electrodisintegration of ^{4}He into ^{3}H and p clusters in three different kinematic setups. The first setup labeled CQ2, in which the electron momentum and energy transfers were kept fixed at $q \simeq 1.43$ GeV and $\omega \simeq 0.52$ GeV, was in quasi-perpendicular kinematics (with the missing momentum $\mathbf{p}_m$ close to being perpendicular to $\mathbf{q}$), while the remaining two setups labeled PY1 and PY2 were both in quasi-parallel kinematics (with $\mathbf{p}_m$ close to being parallel to $\mathbf{q}$) and both covered the same range $0 \lesssim p_m \lesssim 500$ MeV/c, but the electron beam energy and scattering angle were, respectively, about 2.4 GeV and 16.9° in PY1 and about 3.2 GeV and 18.9° in PY2.

In Figs. 9–11 we show for both experiment and theory the reduced cross section, defined as

$$\sigma^{\rm red} = \frac{1}{p\,E\,f_{\rm rec}\,\sigma_{ep}^{\rm CC1}}\,\frac{d^5\sigma}{dE'_e d\Omega'_e d\Omega}\ , \tag{28}$$

where $\sigma_{ep}^{\rm CC1}$ denotes the CC1 off-shell parameterization of the electron-proton cross section

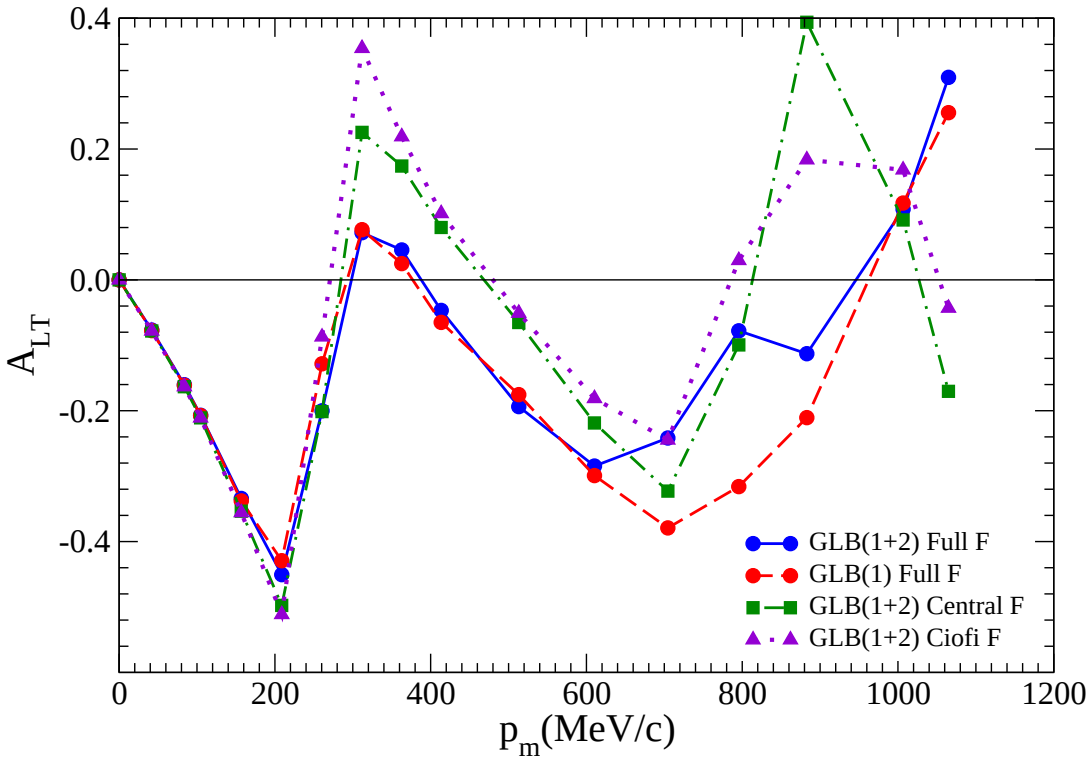

FIG. 8. (Color online) Same as Fig. 4, but for the longitudinal-transverse asymmetry.

due to deForest [36]. The various curves are labeled as follows: "PWIA" represents the plane wave impulse approximation, "GLB with (no) MEC" treats FSI in the Glauber approximation with (without) MEC, "OPT with (no) MEC" uses the optical potential to account for FSI with (without) MEC, and finally the experimental data are labeled by the experiment number "E97-111". We note that the calculations in the Glauber approximation include single, double and triple rescattering (see Sec. II A).

The three kinematic setups all cover the region of missing momentum close to 450 MeV/c, where the PWIA results are orders of magnitude smaller than the data. In PWIA the cross section is proportional to the p-^{3}H cluster momentum distribution, which exhibits a node for p_m close to 450 MeV/c [37]. This node is filled in by FSI contributions, which shift PWIA strength from the low p_m region to the high p_m one, see Figs. 10–11. The contributions from MEC are significant, particularly for kinematics CQ2, and increase the

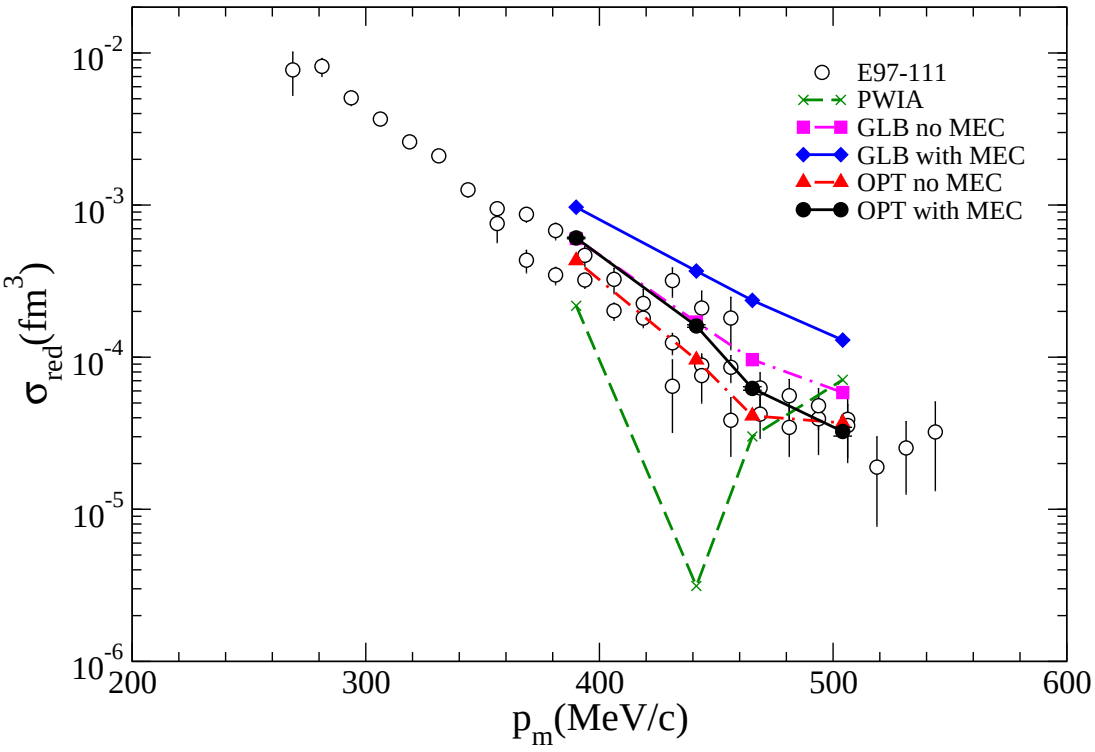

FIG. 9. (Color online) Reduced differential cross section of ^{4}He$(e,e'p)^3$H compared to experimental data and various calculation schemes. "CQ2" refers to the experimental kinematics. See text for descriptions of the curves. Lines are drawn to guide the eye.

cross section over the whole p_m range of interest. The full calculations, including FSI either in the Glauber approximation or via the optical potential and MEC contributions, are in reasonable agreement with data for kinematics PY1 and PY2, although they both tend to overpredict the measured cross sections at low p_m (but not as severely as the PWIA calculation). For kinematics CQ2, the "OPT with MEC" calculation provides a satisfactory description of data, while the "GLB with MEC" calculation leads to cross sections which are significantly larger than the measured values. We note that for kinematics CQ2 the relative kinetic energy between the proton and triton clusters is about 0.31 GeV, so well within the range of applicability of the optical potential, which was fitted to p-^{3}H scattering data up to relative kinetic energy of 0.45 GeV (Sec. II B). In contrast, the proton lab kinetic energies for

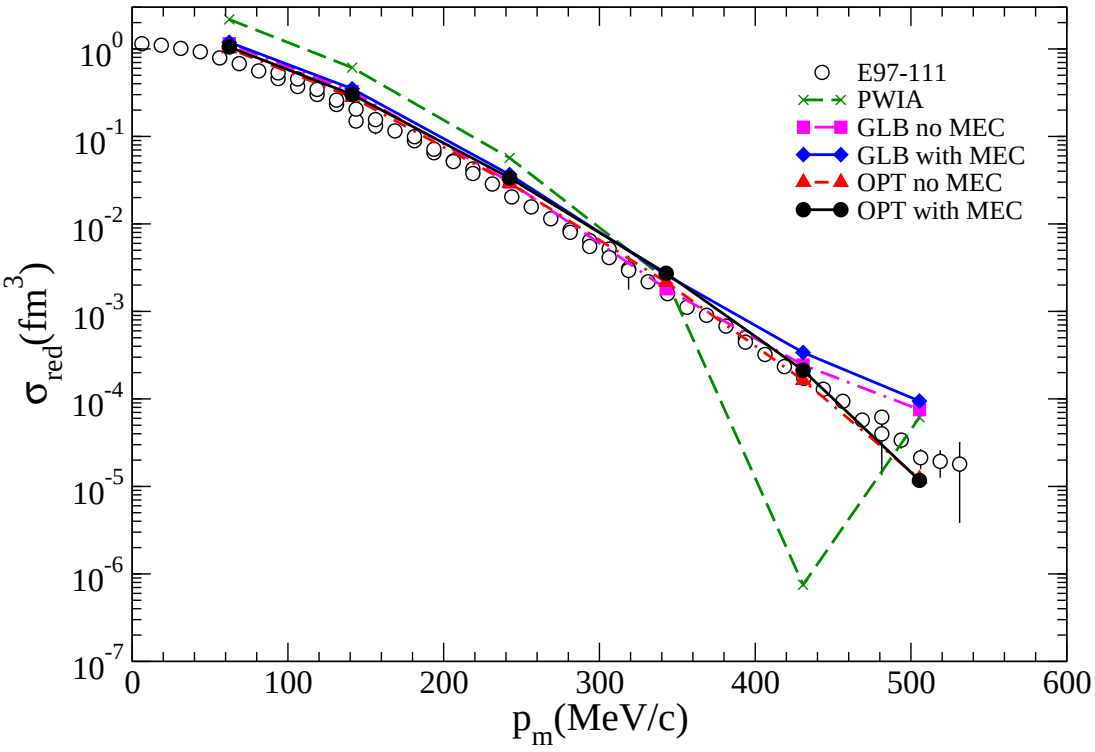

FIG. 10. (Color online) Same as Fig. 9 except for "PY1" kinematics.

this same kinematic setup are of the order of 0.46 GeV, arguably too low for the validity of the Glauber approximation. For the quasi-parallel kinematics PY1 (PY2) the p-^{3}H relative kinetic energies and proton lab kinetic energies are, respectively, in the ranges 0.22–1.05 (0.44–1.55) GeV and 0.34–0.98 (0.51–1.42) GeV, as the missing momentum increases from $\simeq$ 0.06 GeV/c to $\simeq$ 0.5 GeV/c, and therefore one would expect the treatment of FSI via the optical potential to be valid on the low side of p_m and that based on the Glauber approximation to be appropriate for the high side of p_m. In fact, the actual calculations shown in Figs. 10–11 indicate that the optical potential and Glauber approximation differ significantly only beyond $p_m \gtrsim 400$ MeV/c, with the "OPT with MEC" and "GLB with MEC" results, respectively, underestimating and overestimating the data.

We now turn our attention to the polarization observables in the ^{4}He$(\vec{e}, e'\vec{p})^3$H reaction. We present the induced polarization P_y in Fig. 12, and the super-ratio $(P'_x/P'_z)/(P'_x/P'_z)_{\rm PWIA}$

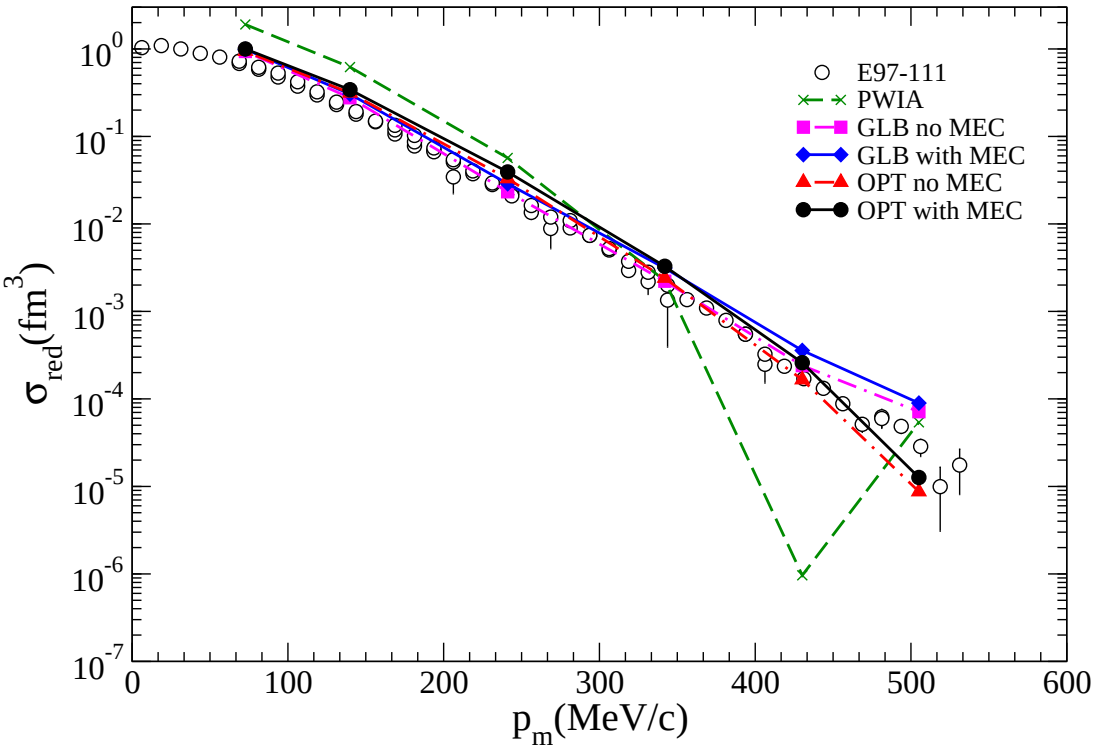

FIG. 11. (Color online) Same as Fig. 9 except for "PY2" kinematics.

in Fig. 13.

These are both plotted versus the four momentum transfer of the virtual photon, Q^2. These observables are compared with data labeled according to the experiment. In Fig. 12 the data labeled "E03-104" are from Ref. [5], and "E93-049" are from Ref. [3]. In Fig. 13 the data labeled "E03-104" are from Ref. [4], "E93-049" are from Ref. [3], and "MAMI" are from Ref. [38]. When comparing to the JLab experimental data we should be mindful that these are averaged over the acceptance of the spectrometers. The super-ratio is only mildly affected by this [39], however the induced polarization can vary substantially. According to Ref. [5] the correction is $\lesssim 20\%$, and additional details of how the correction is made can be found in that work. In the figures, the curves labeled "OPT(no CH-EX)" and "OPT" both use one-body electromagnetic currents, the only difference being that in the "OPT(no CH-EX)" calculation the charge-exchange terms in the optical potential are ignored. The curves

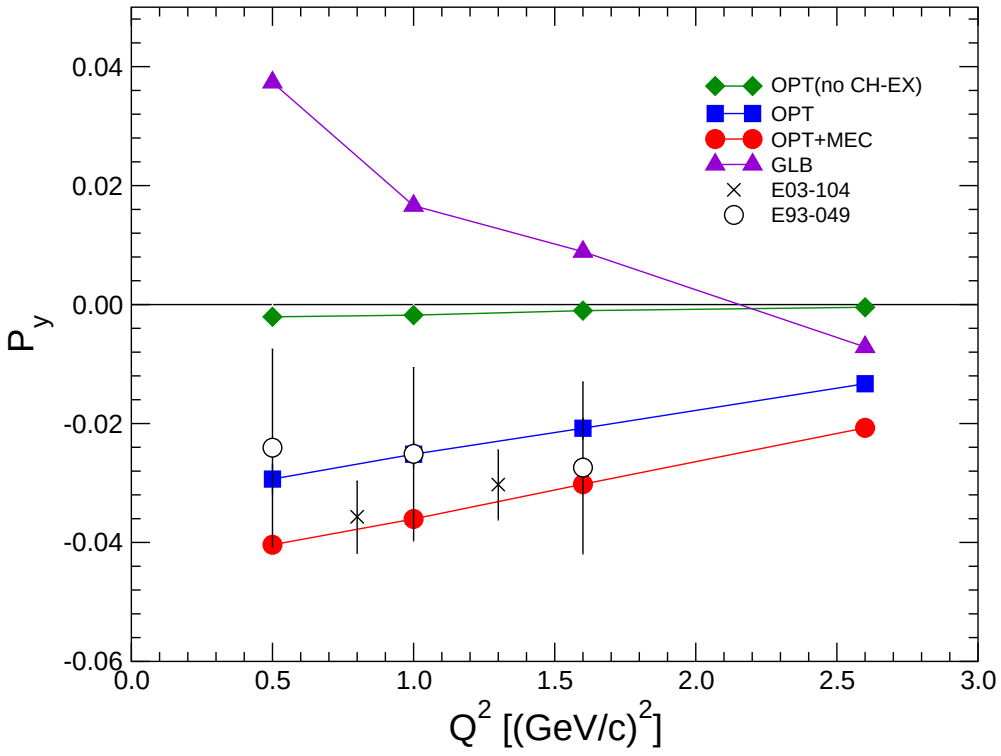

FIG. 12. (Color online) Induced polarization for ^{4}He compared to experimental data. The optical potential is tuned to reproduce the data. See text for descriptions of the curves. Lines are drawn to guide the eye.

labeled "OPT+MEC" include the full optical potential as well as the MEC contributions, while the curves labeled "GLB" correspond to results obtained in the Glauber approximation with one-body currents. The statistical errors associated with the Monte Carlo integrations are only shown for the "OPT+MEC" calculation, they are similar in the other cases. Note that these errors are smaller than those reported in Ref. [15] because of the larger number of configurations in the present random walk.

The present calculation differs from that reported in Ref. [15] in two respects: i) the spin-orbit term in the optical potential, which is poorly determined [15], has been constrained here by fitting the precise induced polarization data obtained in Ref. [5], and ii) calculations of the super-ratio and induced polarization have also been carried out in the Glauber approximation

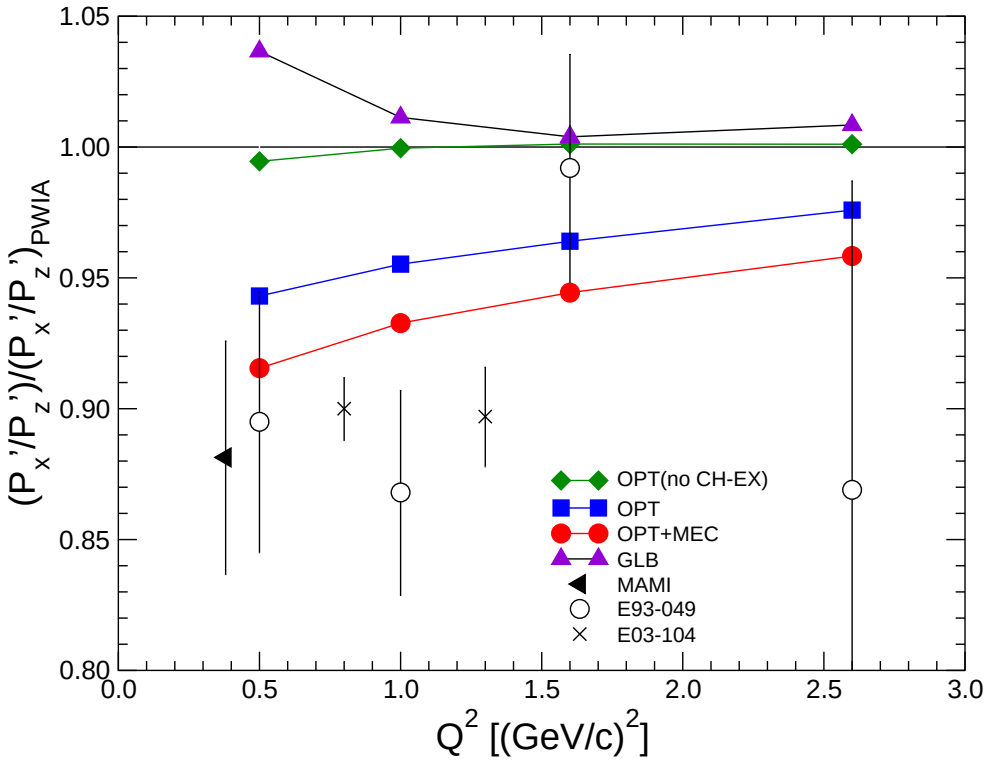

FIG. 13. (Color online) Polarization transfer for ^{4}He compared to experimental data. See text for descriptions of the curves. Lines are drawn to guide the eye.

(including up to triple rescattering). In reference to the calculations based on the optical potential the discussion and ensuing conclusions are similar to those presented in the older study [15]: i) charge-exchange FSI effects are important, ii) the predicted quenching of the super-ratio relative to one comes about because of these effects and because of MEC contributions, and iii) this quenching is in reasonable agreement with that observed in the older [3] as well as in the more recent and accurate [4] data.

The "GLB" calculation is at variance with data, particularly at lower Q^2. While it reproduces the magnitudes of the observables, it has the wrong sign for P_y and increases the super-ratio relative to one. However, we note that for the data in the low Q^2 region the proton lab kinetic energies may be too small for the viability of the Glauber treatment of FSI, for example at $Q^2 = 1$ (GeV/c)^2 this energy is $\simeq 0.55$ GeV.

VI. CONCLUSIONS

In this study we have expanded and built upon the work of Refs. [14, 15], and have calculated observables for the processes ^{3}He$(e,e'p)^2$H and ^{4}He$(e,e'p)^3$H. We have updated the NN amplitudes, which describe FSI within a Glauber approximation, to include more realistic parameterizations available from SAID, valid over the entire angular region. In addition to the SAID parameterizations we also implemented a minimal NN amplitude, which includes no spin dependence and is only valid in the forward direction, allowing for a valuable analysis of the NN model dependence entering the calculation. Comparisons were made to available experimental data, and the theoretical results are in good agreement with them.

In the case of the ^{3}He$(e,e'p)^2$H reaction we have compared several model-dependent effects which can affect the results significantly. Among these effects, FSI are of utmost importance. Contributions from MEC, while small in some cases, can play a large role in other observables or kinematical regimes. We also investigated the importance of including both the full spin dependence in the profile operator and double rescattering in the Glauber approximation. Neglecting either of these effects will have a detrimental impact on the calculation.

For the ^{4}He$(e,e'p)^3$H reaction we found that the results obtained with either the optical potential or Glauber approximation provide a good description of the data obtained in quasi-parallel kinematics (PY1 and PY2). In contrast, the Glauber results overestimate the data in quasi-perpendicular kinematics (CQ2). In reference to the polarization observables measured in the ^{4}He$(\vec{e},e'\vec{p})^3$H reaction, the Glauber results appear to be severely at variance with data on the induced polarization P_y and super-ratio $(P'_x/P'_z)/(P'_x/P'_z)_{\rm PWIA}$, particularly at low Q^2. In contrast, these data are reproduced reasonably well in the calculation based on the optical potential, provided the latter accounts for charge-exchange FSI effects, i.e., the coupling between the p-^{3}H and n-^{3}He channels.

ACKNOWLEDGMENTS

We would like to thank R.A. Arndt and R.L. Workman for correspondence in regard to the use of the SAID interactive program, C. Ciofi degli Atti and H. Morita for the correspondence

regarding their NN parameterization, and D. Higinbotham and B. Reitz, and M. Paolone, S. Malace and S. Strauch, for providing us with tables of the experimental data for the ^{4}He$(e,e'p)^3$H and ^{4}He$(\vec{e},e'\vec{p})^3$H reactions, respectively. This work was supported by the U.S. Department of Energy, Office of Nuclear Physics, under contract DE-AC05-06OR23177. The calculations were made possible by grants of computing time from the National Energy Research Scientific Computing Center.

Appendix A: NN scattering amplitudes

This work requires the NN scattering amplitudes as input to describe the FSI. Here we use the NN amplitudes $\overline{F}_m^{NN}(s,t)$ from Eq. (10), which are in the Wallace representation [21, 40], to produce the profile functions given by Eq. (13). We use a complete set of amplitudes obtained from the SAID analysis and a central (no spin dependence) amplitude from Ciofi and Morita [6–8, 41–47]. Some comments are necessary for each of these choices to clarify their usage in the present work.

It is possible to obtain NN scattering amplitudes in two-dimensional spinor space directly from SAID in the form of the Saclay amplitudes which can be easily related to the Wallace form. The problem with this is that for lab kinetic energies below 350 MeV these are not in agreement with those obtained from the Nijmegen analysis (http://nn-online.org/). However, helicity amplitudes can also be obtained directly from SAID and these can then be converted to Saclay amplitudes, which are in agreement with the Nijmegen analysis. As a result, we start from the SAID helicity amplitudes. These are then converted to the Fermi invariant amplitudes of Eq. (11) as described in Ref. [48]. The coefficients of the Fermi invariant amplitudes are saved as tables of the five invariant amplitudes and as a function of c.m. angle for laboratory kinetic energies T_{lab} from 0.05 GeV to 1.3 GeV for pn scattering and 0.05 GeV to 3.0 GeV for pp scattering. These tables are interpolated using bicubic splines to obtain scattering amplitudes at any energy and angle within the tabulated energy range. These invariant amplitudes have been used successfully to calculate a number of deuteron electrodisintegration observables [48–50]. For the current work the Fermi invariants are converted to Wallace amplitudes by multiplication by an appropriate matrix. Some care has to be used in implementing this approach due to a problem with the production of the helicity amplitudes by SAID. In extracting the amplitudes we have

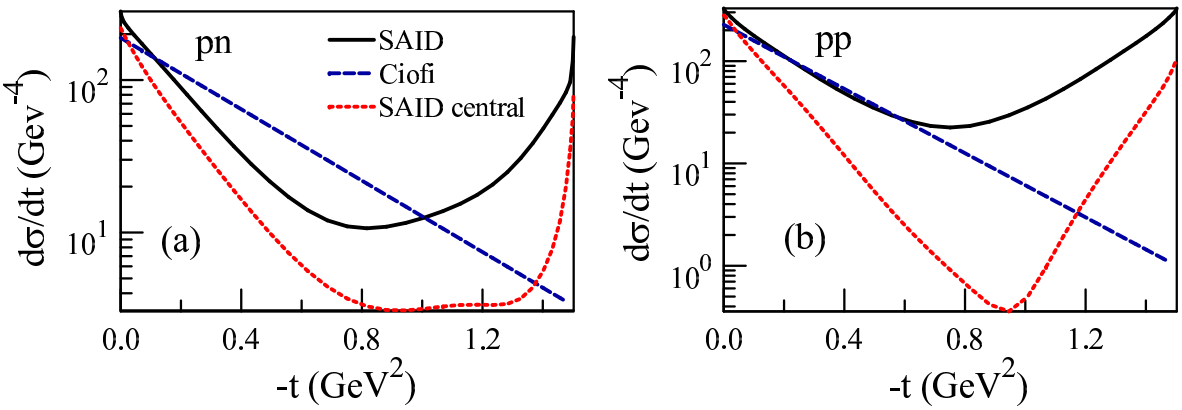

FIG. 14. (color online) Differential cross sections obtained from the SAID (solid line), Ciofi (dashed line) and the central contribution from SAID (short dashed line) amplitudes for (a) pn scattering and (b) pp scattering for $T_{lab} = 0.8$ GeV ($s = 5.03$ GeV^2).

specified that at each energy these are given from $\theta_{c.m.} = 0°$ to 180° in steps of 5°. The resulting amplitudes show a very strong variation at angles near both endpoints resulting in differential cross sections that have large spikes near 0° and 180° that are inconsistent with the scattering data. To eliminate this problem, amplitudes at 5° and 10° are replaced by values obtained from a cubic polynomial fixed by data at 0°, 15°, 20° and 25°. This produces differential cross sections that are in agreement with data.

Ciofi and Morita use only a single spin-independent amplitude of the form

$$\overline{F}_1^{NN}(s, \bar{\boldsymbol{k}}^2) = -i\,\sigma_{tot}(s)\,[1 - i\alpha(s)]\,\mathrm{e}^{-\beta\,\bar{\boldsymbol{k}}^2} \tag{A1}$$

where σ_{tot} is the total NN cross section, α is a ratio of the real to imaginary part of the forward scattering amplitude (often referred to as ρ) and β is determined by calculating the total elastic cross section from Eq. (A1) giving

$$\beta = \frac{\sigma_{tot}^2(s)}{32\pi\,\sigma_{el}^2(s)}\,\left[1 + \alpha^2(s)\right]\,. \tag{A2}$$

The quantities σ_{tot}, $\alpha = \rho$ and σ_{el} can be obtained from either the PDG or from SAID. Differential cross sections using the SAID and Ciofi amplitudes are shown for pn scattering in Fig. 14(a) and for pp scattering in Fig. 14(b) for the full kinematically allowed range in $t = -\bar{\boldsymbol{k}}^2$. Note that while the SAID and Ciofi results are similar in the forward direction for pp scattering, this is not the case for pn scattering. The problem here is in determining

β. The total elastic cross section for pp scattering is completely described by integrating from 0° to 90° since for indistinguishable protons each scattering in the c.m. frame will result in one proton in the forward direction and one in the backward direction. This is not the case for pn scattering since a forward scattering proton will be associated with a backward scattering neutron and a backward scattering proton will be associated with a forward scattering neutron. The total elastic pn cross section requires integration from 0° to 180°. In the case of Fig. 14(b) the total pp elastic cross section corresponds to integrating the differential cross section over half of the range in t, while for Fig. 14(a) the total pn elastic cross section corresponds to integrating the differential cross section over the complete range in t. By including the contributions from backward scattering protons, the total pn elastic cross section is larger than would be required to fit the data in the forward direction resulting in a smaller value of β as given by Eq. (A2). Note also that the values of the cross section calculated from the Ciofi amplitudes are smaller than those obtained from the SAID amplitudes at $t = 0$ due to the contributions from spin-dependent amplitudes at this point.

The third calculation shown in Figs. 14(a) and 14(b) shows the contribution of only the central part of the SAID amplitudes to the differential cross section. This clearly shows that the spin-dependent amplitudes provide a significant part of the cross section and that the method used by Ciofi transfers part of this strength into the central amplitude.

Fortran90 modules are available from Ford and Van Orden (FVO) which calculate the invariant functions, $\mathcal{F}_m^{NN}(s,t)$, given in Eq. (11). The subroutines can provide the amplitudes for a variety of models depending on the energies desired as well as the complexity of the model. At a basic level there is a parametrization available from Ciofi and Morita [6–8, 41–47] describing the NN system with a single amplitude with no spin dependence. Using this amplitude provides a useful comparison for studying how the FSI model dependence, specifically spin dependence, contributes to a calculation. Next one can choose the Wallace parametrization [21], which incorporates spin dependence, but is only valid at small angles. This model was utilized in an earlier work [14] but, due to the limitation above, is not used in this work. There are two parametrizations available which include all spin dependence and are valid over the entire angular region. These are the SAID model [18–20] valid for $s < 5.4$ (GeV^2), and a Regge model [51] valid for $s > 5.4$ (GeV^2). In this work we consider all spin dependence of the FSI, and the energies of interest are those of the SAID approach. For all models the amplitudes are converted first into Fermi invariant functions with a consistent

normalization. The Fermi invariants from any model can be used directly or converted to helicity amplitudes, Saclay amplitudes or Wallace amplitudes.

As discussed above, for the SAID analysis the five independent helicity amplitudes can be obtained on a tabulated grid for the c.m. energy ($\overline{E}$) and angle ($\overline{\theta}$). For convenience we work with the Mandelstam variables which are related to the NN c.m. energy and angle by

$$s = 4\overline{E}^2 \tag{A3}$$

$$t = -\overline{\mathbf{k}}^2 = -\frac{s - 4\,m^2}{2}[1 - \cos(\overline{\theta})]. \tag{A4}$$

If the amplitudes are extracted in units of fm there is a normalization relation between the SAID and FVO conventions,

$$T^{FVO}_{\lambda_1',\lambda_2';\lambda_1,\lambda_2}(s,t) = -\frac{4\pi\sqrt{s}}{\hbar c\, m^2} T^{SAID}_{\lambda_1',\lambda_2';\lambda_1,\lambda_2}(s,t) \tag{A5}$$

The invariants can then be obtained using,

$$\begin{pmatrix} \mathcal{F}_S^{NN}(s,t) \\ \mathcal{F}_V^{NN}(s,t) \\ \mathcal{F}_T^{NN}(s,t) \\ \mathcal{F}_P^{NN}(s,t) \\ \mathcal{F}_A^{NN}(s,t) \end{pmatrix} = \frac{1}{s - 4\,m^2} M^{HtoI} \begin{pmatrix} T_{\frac{1}{2},\frac{1}{2};\frac{1}{2},\frac{1}{2}}(s,t) \\ T_{\frac{1}{2},\frac{1}{2};\frac{1}{2},-\frac{1}{2}}(s,t) \\ T_{\frac{1}{2},-\frac{1}{2};\frac{1}{2},-\frac{1}{2}}(s,t) \\ T_{\frac{1}{2},\frac{1}{2};-\frac{1}{2},-\frac{1}{2}}(s,t) \\ T_{\frac{1}{2},-\frac{1}{2};-\frac{1}{2},\frac{1}{2}}(s,t) \end{pmatrix}, \tag{A6}$$

where the matrix M^{HtoI} and additional details of this discussion can be found in the Appendix of Ref. [48].

Once the invariant functions are obtained we need to represent the amplitudes in the Wallace form so that the Glauber profile operator can be calculated. Normalization between the FVO convention and the convention used in this work is given as,

$$T_{\lambda_1',\lambda_2';\lambda_1,\lambda_2}(s,t) = \frac{i\hbar c\, m^2}{2\pi\sqrt{s(s - 4\,m^2)}} T^{FVO}_{\lambda_1',\lambda_2';\lambda_1,\lambda_2}(s,t) \tag{A7}$$

It is straightforward to transform from the invariant functions to the Wallace form via another matrix multiplication,

$$\begin{pmatrix} \overline{F}_1^{NN}(s,t) \\ \overline{F}_2^{NN}(s,t) \\ \overline{F}_3^{NN}(s,t) \\ \overline{F}_4^{NN}(s,t) \\ \overline{F}_5^{NN}(s,t) \end{pmatrix} = \frac{i\hbar c\, m^2}{2\pi\sqrt{s(s - 4\,m^2)}} M^{ItoW} \begin{pmatrix} \mathcal{F}_S^{NN}(s,t) \\ \mathcal{F}_V^{NN}(s,t) \\ \mathcal{F}_T^{NN}(s,t) \\ \mathcal{F}_P^{NN}(s,t) \\ \mathcal{F}_A^{NN}(s,t) \end{pmatrix}, \tag{A8}$$

where the matrix M^{ItoW} is given below and was obtained from [40]. In Appendix B we show how these amplitudes can be boosted to the rescattering frame (which is in practice taken as the lab frame, see discussion in Sec. II A), and the profile operator can then be calculated from the boosted amplitudes. The matrix elements are:

$$
\begin{aligned}
M_{11}^{ItoW} &= \frac{(-4m^2 - 2m\sqrt{s} + t)^2}{4m^2(2m + \sqrt{s})^2} \\
M_{12}^{ItoW} &= \frac{(-16m^4 - 16m^3\sqrt{s} + 2s^2 + 3st + t^2 + 4m^2(s+t) + 8m\sqrt{s}(s+t))}{4m^2(2m + \sqrt{s})^2} \\
M_{13}^{ItoW} &= \frac{t(4m\sqrt{s} + 2s + t)}{2m^2(2m + \sqrt{s})^2} \\
M_{14}^{ItoW} &= 0 \\
M_{15}^{ItoW} &= \frac{(4m^2 - s - t)t}{4m^2(2m + \sqrt{s})^2} \\
M_{21}^{ItoW} &= \frac{t(-4m^2 + s + t)}{4m^2(2m + \sqrt{s})^2} \\
M_{22}^{ItoW} &= \frac{t(4m\sqrt{s} + 2s + t)}{4m^2(2m + \sqrt{s})^2} \\
M_{23}^{ItoW} &= \frac{-16m^4 - 16m^3\sqrt{s} + 2s^2 + 3st + t^2 + 4m^2(s+t) + 8m\sqrt{s}(s+t)}{2m^2(2m + \sqrt{s})^2} \\
M_{24}^{ItoW} &= 0 \\
M_{25}^{ItoW} &= -\frac{(-4m^2 - 2m\sqrt{s} + t)^2}{4m^2(2m + \sqrt{s})^2} \\
M_{31}^{ItoW} &= \frac{(4m^2 + 2m\sqrt{s} - t)\sqrt{-4m^2 + s + t}}{4m^2(2m + \sqrt{s})^2} \\
M_{32}^{ItoW} &= -\frac{(4m^2 + 6m\sqrt{s} + 2s + t)\sqrt{-4m^2 + s + t}}{4m^2(2m + \sqrt{s})^2} \\
M_{33}^{ItoW} &= -\frac{(4m^2 + 6m\sqrt{s} + 2s + t)\sqrt{-4m^2 + s + t}}{2m^2(2m + \sqrt{s})^2} \\
M_{34}^{ItoW} &= 0 \\
M_{35}^{ItoW} &= \frac{(-4m^2 - 2m\sqrt{s} + t)\sqrt{-4m^2 + s + t}}{4m^2(2m + \sqrt{s})^2} \\
M_{41}^{ItoW} &= \frac{-4m^2 + s + t}{4m^2(2m + \sqrt{s})^2} \\
M_{42}^{ItoW} &= \frac{4m\sqrt{s} + 2s + t}{4m^2(2m + \sqrt{s})^2} \\
M_{43}^{ItoW} &= \frac{4m\sqrt{s} + 2s + t}{2m^2(2m + \sqrt{s})^2}
\end{aligned}
$$

$$
\begin{aligned}
M_{44}^{ItoW} &= -\frac{1}{4m^2} \\
M_{45}^{ItoW} &= \frac{8m^2+4m\sqrt{s}-t}{4m^2(2m+\sqrt{s})^2} \\
M_{51}^{ItoW} &= \frac{(4m^2-s-t)t}{4m^2(2m+\sqrt{s})^2} \\
M_{52}^{ItoW} &= \frac{(4m^2-s-t)t}{4m^2(2m+\sqrt{s})^2} \\
M_{53}^{ItoW} &= -\frac{-32m^4-32m^3\sqrt{s}+2s^2+4m^2t+3st+t^2+8m\sqrt{s}(s+t)}{2m^2(2m+\sqrt{s})^2} \\
M_{54}^{ItoW} &= 0 \\
M_{55}^{ItoW} &= \frac{32m^4+32m^3\sqrt{s}-2s^2-12m^2t-st+t^2-8m\sqrt{s}(s+t)}{4m^2(2m+\sqrt{s})^2} \ .
\end{aligned}
\tag{A9}
$$

Appendix B: From the c.m. to the lab frame

The elastic scattering amplitude in the lab frame is written as

$$
(2\mathrm{i}\,p)^{-1}\,F_{ij}^{NN}(\mathbf{k},s) = \sum_{m=1}^{8} F_m^{NN}(s,\mathbf{k}^2)O_{ij}^m \ , \tag{B1}
$$

where the eight operators O_{ij}^m are taken as

$$
O_{ij}^{m=1,\ldots,8} = 1\,,\ \boldsymbol{\sigma}_i{\cdot}\boldsymbol{\sigma}_j\,,\ \mathrm{i}\,\boldsymbol{\sigma}_i{\cdot}\mathbf{k}{\times}\hat{\mathbf{p}}\,,\ \mathrm{i}\,\boldsymbol{\sigma}_j{\cdot}\mathbf{k}{\times}\hat{\mathbf{p}}\,,\ \boldsymbol{\sigma}_i{\cdot}\mathbf{k}\,\boldsymbol{\sigma}_j{\cdot}\mathbf{k}\,,\ \boldsymbol{\sigma}_i{\cdot}\hat{\mathbf{p}}\,\boldsymbol{\sigma}_j{\cdot}\hat{\mathbf{p}}\,,\ i\,\boldsymbol{\sigma}_i{\cdot}\mathbf{k}\,\boldsymbol{\sigma}_j{\cdot}\hat{\mathbf{p}}\,,\ i\,\boldsymbol{\sigma}_i{\cdot}\hat{\mathbf{p}}\,\boldsymbol{\sigma}_j{\cdot}\mathbf{k}\,. \tag{B2}
$$

Here $\mathbf{p}$ is the momentum of the initial fast nucleon and in the eikonal limit the momentum transfer $\mathbf{k}$ is perpendicular to $\mathbf{p}$. The functions $F_{m=1,\ldots,8}^{NN}$ are then obtained as linear combinations of the invariant functions $\mathcal{F}_{m=1,\ldots,5}^{NN}$,

$$
F_m^{NN} = \sum_{n=1}^{5} L_{mn}\,\mathcal{F}_n^{NN} \ , \tag{B3}
$$

where the $8{\times}5$ matrix L is given by

$$L = \begin{bmatrix} 1-\frac{p^2}{w_p w_{p-k}} & 1+\frac{p^2}{w_p w_{p-k}}+\frac{k^2}{w_{p-k} w_k} & -\frac{2k^2}{w_{p-k} w_k} & 0 & 0 \\ 0 & -\frac{k^2}{w_{p-k} w_k} & 2\left(1+\frac{p^2}{w_p w_{p-k}}+\frac{k^2}{w_{p-k} w_k}\right) & 0 & -1+\frac{p^2}{w_p w_{p-k}} \\ \frac{p}{w_p w_{p-k}} & -\frac{p}{w_p w_{p-k}}\left(1+\frac{w_-}{w_k}\right) & -\frac{2p}{w_p w_{p-k}}\frac{w_+}{w_k} & 0 & 0 \\ 0 & -\frac{p}{w_p w_{p-k}}\frac{w_+}{w_k} & -\frac{2p}{w_p w_{p-k}}\left(1+\frac{w_-}{w_k}\right) & 0 & -\frac{p}{w_p w_{p-k}} \\ 0 & \frac{1}{w_{p-k} w_k} & -\frac{2}{w_{p-k} w_k} & -\frac{1}{w_{p-k} w_k} & -\frac{1}{w_{p-k} w_k} \\ 0 & 0 & -\frac{4p^2}{w_p w_{p-k}} & 0 & -\frac{2p^2}{w_p w_{p-k}} \\ 0 & -i\frac{p}{w_p w_{p-k}}\frac{w_-}{w_k} & -i\frac{2p}{w_p w_{p-k}}\left(1+\frac{w_+}{w_k}\right) & 0 & -i\frac{p}{w_p w_{p-k}} \\ 0 & 0 & -i\frac{2p}{w_p w_{p-k}} & -i\frac{p}{w_p w_{p-k}}\frac{w_-}{w_k} & -i\frac{p}{w_p w_{p-k}}\left(1+\frac{w_+}{w_k}\right) \end{bmatrix} ,$$

and the factors E_q and w_q are defined as $E_q \equiv \sqrt{\mathbf{q}^2 + m^2}$ and $w_q \equiv E_q + m$, with $\mathbf{q} = \mathbf{p}$, $\mathbf{k}$, $\mathbf{p} - \mathbf{k}$, and $w_\pm \equiv w_{p-k} \pm w_p$,

The NN profile operator Γ_{ij}^{NN} is obtained from Eq. (13) by replacing $\Gamma_{ij}^{(m)}$ with $\Gamma_{NN}^{(m)}$ for $m = 1, \ldots, 8$. The functions $\Gamma_{NN}^{(m)}$ are in turn derived from Bessel transforms of the F_m^{NN} amplitudes. We find:

$$\Gamma_{NN}^{(m)}(b;s) = 2\,p^2 \int_{-1}^{1} \mathrm{d}x\, J_0(kb)\, F_m^{NN}(k^2;s) \tag{B4}$$

for $m = 1, 6$;

$$\Gamma_{NN}^{(m)}(b;s) = \frac{2\,p^2}{b} \int_{-1}^{1} \mathrm{d}x\, k\, J_1(kb)\, F_m^{NN}(k^2;s) \tag{B5}$$

for $m = 3, 4, 7, 8$; and lastly

$$\Gamma_{NN}^{(2)}(b;s) = 2\,p^2 \int_{-1}^{1} \mathrm{d}x\, J_0(kb)\, F_2^{NN}(k^2;s) + \frac{2\,p^2}{b} \int_{-1}^{1} \mathrm{d}x\, k\, J_1(kb)\, F_5^{NN}(k^2;s)\ , \tag{B6}$$

$$\Gamma_{NN}^{(5)}(b;s) = \frac{2\,p^2}{b^2} \int_{-1}^{1} \mathrm{d}x\, k^2 \left[J_0(kb) - \frac{2}{k\,b} J_1(kb)\right] F_5^{NN}(k^2;s)\ . \tag{B7}$$

In obtaining the integrals above, we made the variable change $k \to 2\,p \sin(\theta/2) = 2\,p\,\sqrt{(1-x)/2}$ with $x = \cos\theta$.

---

[1] M. M. Rvachev *et al.* (Jefferson Lab Hall A Collaboration), Phys. Rev. Lett. **94**, 192302 (2005).

[2] B. Reitz (for the Jefferson Lab Hall A Collaboration), Eur. Phys. J. **A19**, S1, 165 (2004).

[3] S. Strauch *et al.*, Phys. Rev. Lett. **91**, 052301 (2003).

[4] M. Paolone *et al.* (E03-104 Collaboration), Phys. Rev. Lett. **105**, 072001 (2010).

[5] S. P. Malace *et al.* (E03-104 Collaboration), Phys. Rev. Lett. **106**, 052501 (2011).

[6] C. C. degli Atti and L. P. Kaptari, Phys. Rev. C **71**, 024005 (2005).

[7] C. Ciofi degli Atti and L. P. Kaptari, Phys. Rev. Lett. **95**, 052502 (2005).

[8] C. C. degli Atti and L. P. Kaptari, Phys. Rev. Lett. **100**, 122301 (2008).

[9] M. Alvioli, C. C. d. Atti, and L. P. Kaptari, Phys. Rev. C **81**, 021001 (2010).

[10] J. M. Laget, Phys. Rev. C **72**, 024001 (2005).

[11] J. Laget, Physics Letters B **609**, 49 (2005).

[12] M. M. Sargsian, T. V. Abrahamyan, M. I. Strikman, and L. L. Frankfurt, Phys. Rev. C **71**, 044614 (2005).

[13] M. M. Sargsian, T. V. Abrahamyan, M. I. Strikman, and L. L. Frankfurt, Phys. Rev. C **71**, 044615 (2005).

[14] R. Schiavilla, O. Benhar, A. Kievsky, L. Marcucci, and M. Viviani, Phys.Rev. **C72**, 064003 (2005).

[15] R. Schiavilla, O. Benhar, A. Kievsky, L. Marcucci, and M. Viviani, Phys.Rev.Lett. **94**, 072303 (2005).

[16] R. B. Wiringa, V. G. J. Stoks, and R. Schiavilla, Phys. Rev. C **51**, 38 (1995).

[17] B. S. Pudliner, V. R. Pandharipande, J. Carlson, and R. B. Wiringa, Phys. Rev. Lett. **74**, 4396 (1995).

[18] R. A. Arndt, I. I. Strakovsky, and R. L. Workman, Phys. Rev. C **62**, 034005 (2000).

[19] R. A. Arndt, W. J. Briscoe, I. I. Strakovsky, and R. L. Workman, Phys.Rev. **C76**, 025209 (2007).

[20] "SAID," `http://gwdac.phys.gwu.edu/`, accessed: 2012-09-21.

[21] S. Wallace, *Advances in Nuclear Physics*, edited by J. Negele and E. Vogt, Vol. 12 (Plenum, New York, 1981) p. 135.

[22] R. Glauber, *Lectures in Theoretical Physics*, edited by W. Brittain and L. Dunham, Vol. 1. (Interscience, New York, 1959).

[23] J. A. McNeil, L. Ray, and S. J. Wallace, Phys. Rev. C **27**, 2123 (1983).

[24] W. T. H. van Oers, B. T. Murdoch, B. K. S. Koene, D. K. Hasell, R. Abegg, D. J. Margaziotis, M. B. Epstein, G. A. Moss, L. G. Greeniaus, J. M. Greben, J. M. Cameron, J. G. Rogers, and A. W. Stetz, Phys. Rev. C **25**, 390 (1982).

[25] R. Schiavilla, Phys. Rev. Lett. **65**, 835 (1990).

[26] M. Viviani, A. Kievsky, and S. Rosati, Phys. Rev. C **71**, 024006 (2005).

[27] S. Jeschonnek and T. W. Donnelly, Phys. Rev. C **57**, 2438 (1998).

[28] J. Carlson and R. Schiavilla, Rev. Mod. Phys. **70**, 743 (1998).

[29] J. Carlson, J. Jourdan, R. Schiavilla, and I. Sick, Phys. Rev. C **65**, 024002 (2002).

[30] L. E. Marcucci, M. Viviani, R. Schiavilla, A. Kievsky, and S. Rosati, Phys. Rev. C **72**, 014001 (2005).

[31] G. Hohler, E. Pietarinen, I. Sabba Stefanescu, F. Borkowski, G. Simon, *et al.*, Nucl.Phys. **B114**, 505 (1976).

[32] E. J. Brash, A. Kozlov, S. Li, and G. M. Huber, Phys. Rev. C **65**, 051001 (2002).

[33] M. K. Jones *et al.* ((The Jefferson Lab Hall A Collaboration)), Phys. Rev. Lett. **84**, 1398 (2000).

[34] A. Raskin and T. Donnelly, Annals of Physics **191**, 78 (1989).

[35] A. Picklesimer and J. W. Van Orden, Phys. Rev. C **40**, 290 (1989).

[36] T. de Forest, Jr., Nuclear Physics A **392**, 232 (1983).

[37] R. Schiavilla, V. Pandharipande, and R. Wiringa, Nuclear Physics A **449**, 219 (1986); R. Wiringa, R. Schiavilla, S. C. Pieper, and J. Carlson, (2013), arXiv:1309.3794 [nucl-th].

[38] S. Dieterich *et al.*, Physics Letters B **500**, 47 (2001).

[39] S. Strauch, Private Communication.

[40] J. A. McNeil, L. Ray, and S. J. Wallace, Phys. Rev. C **27**, 2123 (1983).

[41] H. Morita, M. Braun, C. C. degli Atti, and D. Treleani, Nuclear Physics A **699**, 328 (2002), 3rd Int. Conf. on Perspectives in Hadronic Physics.

[42] C. C. degli Atti, L. Kaptari, and H. Morita, Nuclear Physics A **782**, 191 (2007), proceedings of the 5th International Conference on Perspectives in Hadron Physics, ParticleNucleus and NucleusNucleus Scattering at Relativistic Energies.

[43] H. Morita, Y. Akaishi, O. Endo, and H. Tanaka, Progress of Theoretical Physics **78**, 1117 (1987).

[44] H. Morita, Y. Akaishi, and H. Tanaka, Progress of Theoretical Physics **79**, 1279 (1988).

[45] M. A. Braun, C. Ciofi degli Atti, and D. Treleani, Phys. Rev. C **62**, 034606 (2000).

[46] C. Ciofi degli Atti, L. P. Kaptari, and H. Morita, Few-Body Systems **43**, 39 (2008).

[47] C. Ciofi degli Atti and H. Morita, Private Communication.

[48] S. Jeschonnek and J. W. Van Orden, Phys.Rev. **C78**, 014007 (2008).

[49] S. Jeschonnek and J. W. Van Orden, Phys.Rev. **C81**, 014008 (2010).

[50] S. Jeschonnek and J. W. Van Orden, Phys.Rev. **C80**, 054001 (2009).

[51] W. P. Ford and J. W. Van Orden, Phys. Rev. C **87**, 014004 (2013).